Title

MLKS2 is an ARM domain and F-actin-associated KASH protein that functions in stomatal complex development and meiotic chromosome segregation

Authors

Gumber, Hardeep K.[1]; McKenna, Joseph F.[2]; Tolmie, Andrea F.[2]; Jalovec, Alexis M.[1]; Kartick, Andre C.[1]; Graumann, Katja[2]; Bass, Hank W.[1]

Affiliations

1. Department of Biological Science, Florida State University, Tallahassee, FL, USA, 32306-4295.
2. Department of Biological and Medical Sciences, Faculty of Health and Life Sciences, Oxford Brookes University, Oxford, UK, OX30BP.

Corresponding Author:
Hank W. Bass, bass@bio.fsu.edu

Abstract: The linker of nucleoskeleton and cytoskeleton (LINC) complex is an essential multi-protein structure spanning the eukaryotic nuclear envelope. The LINC complex functions to maintain nuclear architecture, positioning, and mobility, along with specialized functions in meiotic prophase and chromosome segregation. Members of the LINC complex were recently identified in maize, an important scientific and agricultural grass species. Here we characterized *Maize LINC KASH AtSINE-like2*, *MLKS2*, which encodes a highly conserved SINE-group plant KASH protein with characteristic N-terminal armadillo repeats (ARM). Using a heterologous expression system, we showed that actively expressed GFP-MLKS2 is targeted to the nuclear periphery and colocalizes with F-actin and the endoplasmic reticulum, but not microtubules in the cell cortex. Expression of GFP-MLKS2, but not GFP-MLKS2ΔARM, resulted in nuclear anchoring. Genetic analysis of transposon-insertion mutations, *mlks2-1* and *mlks2-2*, showed that the mutant phenotypes were pleiotropic, affecting root hair nuclear morphology, stomatal complex development, multiple aspects of meiosis, and pollen viability. In male meiosis, the mutants showed defects for bouquet-stage telomere clustering, nuclear repositioning, perinuclear actin accumulation, dispersal of late prophase bivalents, and meiotic chromosome segregation. These findings support a model in which the nucleus is connected to cytoskeletal F-actin through the ARM-domain, predicted alpha solenoid structure of MLKS2. Functional conservation of MLKS2 was demonstrated through genetic rescue of the misshapen nuclear phenotype of an Arabidopsis (triple-*WIP*) KASH mutant. This study establishes a role for the SINE-type KASH proteins in affecting the dynamic nuclear phenomena required for normal plant growth and fertility.

Keywords

KASH, LINC, nuclear envelope, actin, FRAP, maize, MLKS2, meiosis, telomere, bouquet

List of abbreviations

FRAP; Fluorescence recovery after photobleaching

DPI; Days post infiltration

OD; Optical density

MLKS2; Maize LINC KASH AtSINE-like2

LINC; Linker of nucleoskeleton and cytoskeleton

NE; Nuclear envelope

INM; Inner nuclear membrane

ONM; Outer nuclear membrane

62 ## Introduction

63 The cell nucleus is a eukaryotic organelle that houses, organizes and expresses the bi-
64 parentally inherited genetic material. As a cellular compartment, the nucleus is
65 separated from the cytoplasm by the multifunctional double-membraned nuclear
66 envelope (NE). The NE has embedded macromolecular protein complexes, such as the
67 nuclear pore complex (NPC) and the linker of nucleoskeleton and cytoskeleton (LINC)
68 complex, which coordinate fundamental cell processes such as signaling and gene
69 regulation (reviewed by Hetzer, 2010; Van de Vosse et al., 2011; D'Angelo, 2018).

70 The LINC complex was discovered relatively recently, but has been shown to be
71 highly conserved in eukaryotes, with myriad functions as described in numerous
72 reviews (Burke and Roux, 2009; Chang et al., 2015; Hieda, 2017; Kim et al., 2015;
73 Luxton and Starr, 2014; Meier et al., 2017). These LINC-mediated functions include
74 regulation of nuclear shape and position (Dittmer and Richards, 2008; Sakamoto and
75 Takagi, 2013), mechanosensory signal transduction (Uzer et al., 2016), control of cell
76 division, intranuclear architecture and gene regulation (Alam et al., 2016; Poulet et al.,
77 2017b; Wang et al., 2018), and the specialized behavior of meiotic chromosomes to
78 ensure segregation and fertility (Link et al., 2014; Murphy et al., 2014; Varas et al.,
79 2015). The two core LINC components are the inner nuclear membrane (INM) SUN-
80 domain proteins (Hagan and Yanagida, 1995; Malone et al., 1999) and outer nuclear
81 membrane (ONM) KASH-domain proteins (Starr and Han, 2002). The SUN domain
82 proteins are relatively well conserved across taxa and can be recognized by sequence
83 homology and domain composition which includes transmembrane domains, the SUN
84 domain, and a coiled-coil domain. In contrast, KASH proteins are functionally

85 conserved, with a C-terminal region that includes a transmembrane domain and
86 diagnostic terminal residues, but otherwise can be quite divergent with limited apparent
87 homology (Zhou and Meier, 2013; Evans et al., 2014; Kim et al., 2015; Meier, 2016;
88 Poulet et al., 2017a).

89 Structural studies reveal that SUN proteins form trimers that can bind to three
90 KASH proteins (Sosa et al., 2012). The cytoplasmic N-terminal regions of KASH domain
91 proteins interact directly or indirectly with a variety of cytoskeletal structures including
92 motor proteins, microfilaments, microtubules, or intermediate filaments (Starr and
93 Fridolfsson, 2010; Tamura et al., 2013; Luxton and Starr, 2014; Varas et al., 2015). The
94 forces generated by the cytoskeletal elements result in LINC-dependent movements
95 known or thought to be required for specialized nuclear morphology associated with
96 mitotic and meiotic cell division, karyogamy at fertilization, cell polarity, and response to
97 biotic and abiotic interactions (Starr and Fridolfsson, 2010; Gundersen and Worman,
98 2013; Griffis et al., 2014; Fernández-Álvarez et al., 2016; Groves et al., 2018).

99 Most of our knowledge of the LINC complex comes from studies of metazoans
100 and yeast. However, given the global challenges in agriculture and the need for plant-
101 based biorenewable resources (Godfray et al., 2010), it is important to better
102 understand the plant NE and its fundamental components. Recently, progress towards
103 understanding plant LINC biology has expanded beyond Arabidopsis to include
104 Medicago and maize (Gumber et al., 2019; Newman-Griffis et al., 2019).

105 The first SUN domain protein identified in plants was OsSad1, found in a nuclear
106 proteomic study in rice (Moriguchi et al., 2005). Subsequently, SUN domain proteins
107 have been identified in many plant species (reviewed by Meier, 2016; Meier et al., 2017;

108 Poulet et al., 2017a) with roles in the maintenance of nuclear shape and size
109 (Graumann et al., 2010; Oda and Fukuda, 2011; Graumann et al., 2014) and meiotic
110 chromosome behavior (Murphy et al., 2014; Varas et al., 2015). In maize, SUN2 has
111 been shown to form a novel structure called the meiotic SUN belt during prophase of
112 meiosis I (Murphy et al., 2014). The SUN belt region of the NE includes the telomere
113 cluster which defines the zygotene bouquet (Murphy et al., 2014).

114 The first plant KASH proteins were originally discovered in Arabidopsis through
115 analysis of RanGAP-NE anchoring proteins, and implicated in NE-associated signaling
116 and maintenance of nuclear shape (Xu et al., 2007; Zhou et al., 2012). They were later
117 shown to bind to SUN (Meier et al., 2010; Zhou et al., 2012) and possess a single near-
118 C-terminal TMD and a C-terminal amino acid sequence of V/P-P-T. These features are
119 diagnostic of plant KASH-like proteins and were collectively used as criteria for
120 identification of ten KASH candidates in maize (Gumber et al., 2019). From that study,
121 four groups of Maize LINC KASH (MLK) related genes were identified: the *AtWIP*-like
122 group (*MLKP1* - *MLKP4*), the *AtSINE*-like group (*MLKS1* and *MLKS2*), the grass-
123 specific group (*MLKG1* and *MLKG2*), and the KASH-associated *AtWIT*-like group
124 (*MLKT1* and *MLKT2*).

125 A particularly interesting and distinct group of plant KASH-like proteins are the
126 SUN-interacting nuclear envelope (SINE) proteins, which contain armadillo domains
127 (Armadillo-type fold, InterPro ID: IPR000225). The armadillo (ARM) type fold is a
128 protein-protein interaction surface formed by twisting of multiple alpha helices around a
129 central axis, and has been reported in a variety of proteins involved in intracellular
130 signalling and cytoskeletal regulation (Coates, 2003; Hatzfeld, 1998). Genetic analysis

131 of the SINE-group KASH genes in Arabidopsis reveals non-redundant functions ranging
132 from actin-dependent nuclear positioning in guard cells for *AtSINE1* to innate immunity
133 against a fungal pathogen for *AtSINE2* (Zhou et al., 2014). Despite their deep
134 conservation, the biological functions of plant SINE-group KASH genes in monocot
135 grass species remain largely uncharacterized. Maize contains two *AtSINE1* homologs,
136 *MLKS1* (Zm00001d031134) and *MLKS2* (Zm00001d052955). Both of these contain an
137 ARM domain towards their N-terminus (Gumber et al., 2019). Given the fundamental
138 importance of connecting the nucleus to the cytoplasm, these maize SINE-group KASH
139 genes were predicted to participate in a broad array of processes requiring coordinated
140 actions of the NE with the cytoskeleton.

141 In this study, we have undertaken an investigation of a single maize LINC gene,
142 *MLKS2,* for several reasons. First of all, the MLKS2 protein was detected in CoIP
143 assays using ZmSUN2 antisera with earshoot nuclei (Gumber et al., 2019). Secondly,
144 *MLKS2* is expressed in actively dividing cells, including meiosis-stage tassels,
145 according to transcriptomic studies (Stelpflug et al., 2016). Thirdly, *MLKS2* orthologs are
146 conserved across land plants, increasing the potential translational impact of the study
147 (Gumber et al., 2019). Finally, two independent Mu transposon insertion alleles of
148 *MLKS2* were available (https://maizegdb.org/uniformmu) allowing for genetic and
149 phenotypic analyses. Here we characterize *MLKS2* using genetic and cellular
150 experiments in order to: (1) test for canonical KASH properties of NE localization and
151 SUN-binding; (2) investigate colocalization with cytoplasmic structures; (3) address its
152 role in meiosis and nuclear shape and positioning via mutant phenotyping; (4) gain
153 mechanistic insight into its role in nuclear positioning and actin interaction using domain

154 deletion assays; and (5) test for functional conservation through cross-species genetic
155 rescue of nuclear shape phenotype.
156

157 ## Results

158

159 The structure of the *MLKS2* gene and protein are summarized in Figure 1. The
160 *MLKS2* gene Zm00001d052955_T001 (from B73 v4) has three exons and is predicted
161 to encode a protein with 637 amino acids (Fig. 1A-B). The secondary and domain
162 structure of the MLKS2 protein includes the canonical KASH features of a single
163 transmembrane domain near the C-terminus, followed by a 14-residue C-terminal KASH
164 domain and terminal sequence of LVPT (Fig. 1C). Nearly half of the protein (8-294) has
165 an armadillo-type fold domain (InterPro IPR016024). Another large segment (301-598)
166 is composed of three segments classified as disordered regions, designated here as
167 DR1 (301-401), DR2 (414-478), and DR3 (488-598). Tertiary structure prediction using
168 I-TASSER revealed that the ARM and disordered regions could adopt a single large
169 structure similar to that of human protein phosphatase 2A, PP2A, a structural
170 scaffolding subunit. PP2A (pdb 1b3uA) was the top ranked structural analog as shown
171 separately and threaded together with MLKS2 (Fig. 1D). This overall structure is
172 referred to as an alpha solenoid, broadly deployed in biological systems as a binding
173 structure (Fournier et al., 2013).
174

175 **Nuclear envelope localization of MLKS2 is disrupted by C-terminal but not ARM**
176 **domain deletions**

177 We first examined the cellular localization of MLKS2 and its potential to interact
178 with SUN or the cytoskeleton. GFP-tagged MLKS2 was transiently expressed and
179 imaged as shown in Figure 2, using the tobacco expression system previously
180 described (Gumber et al., 2019). The GFP-MLKS2 localized to the nuclear periphery as
181 expected for a KASH protein (Fig. 2B). The GFP-MLKS2 was also seen at the cell
182 periphery in a conspicuous pattern resembling that of a cytoskeletal network (Fig. 2B).
183 In order to map the protein regions responsible for these patterns, we made a series of
184 domain deletion constructs (Fig. 2A). The deletions were MLKS2Δ4, with removal of
185 the terminal four amino acid residues; MLKS2ΔKASH, with replacement of the terminal
186 KASH domain with three alanine residues; MLKS2ΔTM, with removal of the
187 transmembrane domain; or MLKS2ΔARM, with removal of the entire Armadillo fold
188 region, DR1, DR2, and part of DR3.
189 We found that the terminal Δ4 and ΔKASH constructs reduced the relative
190 abundance of MLKS2 at the nuclear periphery but retained the network-like pattern in
191 cytoplasm as clearly seen at the cell periphery (arrows, Fig. 2B). In contrast, removal of
192 the TM domain completely changed the localization pattern at both the nuclear and the
193 cell periphery to one resembling that of a soluble protein showing nucleoplasmic and
194 cytoplasmic labelling. The N-terminal deletion construct, ΔARM, retained its NE
195 localization but with a more uniform and less patchy signal. However, the ΔARM variant
196 had a dramatic effect on the cell peripheral labelling, which changed from a filamentous
197 cytoskeleton-like pattern to a more endoplasmic reticulum-like pattern (arrow heads,
198 Fig. 2B), including both sheets and tubules. These results demonstrate that when
199 expressed under the control of a constitutive promoter, MLKS2 can accumulate at two

200 places in the cell, the NE requiring C-terminal domains and the cytoplasm requiring the
201 N-terminal ARM domains. It remains a formal possibility that the non-nuclear
202 cytoplasmic MLKS2 may be an artifact of experimental over- or heterologous
203 expression and may not, therefore, reflect its primary biological function.
204
205 **The KASH and ARM domains immobilize the NE-associated MLKS2**
206 We next tested for interaction of MLKS2 with ZmSUN2 using fluorescence
207 recovery after photobleaching (FRAP). The mobility of GFP-MLKS2 expressed alone
208 was compared to that co-expressed with full length mCherry-ZmSUN2, or deletion
209 constructs lacking the SUN domain or coiled-coil regions of ZmSUN2 (Fig. 2C, D, S1).
210 GFP-MLKS2 has a large immobile fraction to start with, showing only 25% fluorescence
211 recovery 30 s after photobleaching (Fig. 2D). When co-expressed with full length
212 SUN2, the immobile fraction of GFP-MLKS2 showed a slight but statistically insignificant
213 increase compared to GFP-MLKS2 alone (Fig. 2C, D). When co-expressed with SUN2
214 protein lacking the coiled-coil domain (SUN2ΔCC), the immobile fraction of GFP-MLKS2
215 was significantly increased compared to GFP-MLKS2 alone or when co-expressed with
216 full length ZmSUN2. When co-expressed with ZmSUN2 protein lacking the SUN
217 domain (SUN2ΔSUN), the immobile fraction of GFP-MLKS2 was significantly and
218 markedly decreased compared to GFP-MLKS2 alone or when co-expressed with full
219 length ZmSUN2.
220 Given the large immobile fraction of MLKS2 to begin with, we did not expect to
221 observe a marked increase in its immobile fraction when co-expressed with full length
222 SUN. However, the drastic reduction in the immobile fraction when co-expressed with
223 SUN2ΔSUN, compared to co-expression with full-length SUN, was unexpected but

224 consistent with the interpretation that MLKS2 interacts with SUN2 via its SUN domain.
225 One possible explanation for the unexpected effect of the SUN2ΔSUN is that its
226 expression could have a dominant negative effect on the tobacco nuclear envelope
227 components and their ability to interact with GFP-MLKS2. We conclude that two
228 regions of MLKS2 each play a role in anchoring it within the NE, the C-terminal KASH
229 domain and the N-terminal ARM domain.
230 We used the FRAP mobility assay to decipher the contributions of the KASH and
231 ARM domains to the relatively large immobile fraction of MLKS2. Removal of the KASH
232 domain decreased the immobile fraction (Fig. 2E, F, S1), consistent with a KASH-SUN
233 binding interaction in the NE. Remarkably, removal of the ARM domain decreased the
234 immobile fraction even more (Fig. 2E, F) making over 60% of the protein population
235 mobile. This indicates that SINE2-type KASH proteins are likely docked in the NE
236 through interactions at both ends, one via SUN-KASH binding in the NE and one via
237 ARM domain binding to the cytoskeleton.
238
239 **Genetic analysis of two transposon-disrupted alleles of *MLKS2***
240 For genetic analysis, we searched the UniformMu transposon mutagenesis
241 records (McCarty and Meeley, 2009) at maizeGDB and found two alleles for *MLKS2*.
242 The mutator element mobilized in UniformMu is MuDR, a 1.4 kbp non-autonomous *Mu1*
243 element (Barker et al., 1984). The two insertion alleles are designated here as *mlks2-1*
244 and *mlks2-2*, as diagrammed in Figure 3. Both alleles involved insertions into the
245 protein coding region in Exon 2. PCR primers were selected to confirm the location and
246 sequences surrounding the transposon insertion sites (Fig. 3 A,B). For each allele, a 9-

247 bp target site duplication was detected (underlined, Fig. 3B), characteristic for *Mu*
248 insertions. The PCR reactions used for genotyping of individual plants are shown for
249 representative individuals from families segregating for the insertions (Fig. 3C)
250 We examined RNA from immature, meiosis-staged tassels of wild-type and
251 mutant plants to check if the transposon insertions reduced the mRNA levels.
252 Quantitative RT-PCR showed that both alleles, *mlks2-1* and *mlks2-2*, resulted in
253 decreased relative RNA levels when compared to those from wild-type siblings (*Mu -/-*)
254 of *mlks2-1* and *mlks2-2* or those from parental W22 line of maize (Fig. 3D). Of the two
255 alleles, *mlks2-2* showed the greatest reduction in transcript levels.
256
257 ***MLKS2* is required for normal male meiosis and pollen development.**
258 Given the role of the LINC complex and NE in meiosis, we asked whether
259 genetic disruption of *MLKS2* resulted in meiotic or post-meiotic phenotypes. In maize,
260 like most eukaryotes, the NE and the LINC complex have highly specialized functions
261 including a role in telomere bouquet formation, pairing, synapsis, and recombination, all
262 of which must occur with high fidelity to ensure proper genome reduction and euploid
263 transmission. We therefore used 3D cytology to look for several hallmarks of normal
264 male meiosis, including the telomere bouquet, the eccentric positioning of the nucleus at
265 early prophase I, 10 bivalents at late prophase I indicative of complete pairing, chiasma
266 formation, and equal distribution of chromosomes after meiosis I and II as evidenced by
267 daughter nuclei with matching sizes and shapes.
268 The *mlks2-2* mutants showed deviations from all of the cytological meiotic
269 hallmarks inspected as summarized in Figure 4. At early meiotic prophase, 3D

270 telomere FISH revealed that the *mlks2-2* plants showed partial telomere clustering on
271 the NE at the bouquet stage (Fig. 4A-C) with variable numbers (4-12) of telomere FISH
272 signals far removed from the primary cluster (bracketed "bq" in Fig. 4A, B). The
273 magnitude of telomere dispersion was measured using pairwise telomere FISH signal
274 distances per nucleus. The average pairwise telomere distance increased by 50% in
275 the mutant, from 4.3 microns in normal nuclei (n=6) to 6.5 microns in *mlks2-2* nuclei
276 (n=11). The tendency for multiple telomeres to reside far from the bouquet is also seen
277 in the fold change of inter-telomere pairwise distances for the long distance bins (Fig.
278 4C). At early prophase I, meiotic nuclei tend to relocate towards one edge of the cell
279 (Cowan et al., 2002), but *mlks2-2* nuclei remained closer to the cell center (Fig. 4D,E),
280 according to measures of nuclear eccentricity. The cell-to-nucleus centroid offset at
281 early prophase in normal cells decreased from 15 microns in normal (n=6) plants to 7
282 microns in mutant (n=11) plants (Fig. 4F).
283 In the late prophase I stages of diplotene or diakinesis, chromosomes continue to
284 condense while successful disomic pairing and recombination becomes cytologically
285 evident in the form of well-separated bivalents. These bivalents total up to the haploid
286 chromosome number, 10 in the case of normal maize (Fig. 4G). Failure to properly pair
287 or recombine typically results univalents or multivalents, which often fail to segregate
288 properly at anaphase during meiosis I division. The *mlks2-2* mutation caused
289 conspicuous and obvious departure from these normal late prophase I patterns (Fig.
290 4H-J). The meiotic chromosomes from mutant plants showed aggregation and
291 pronounced clumping of multiple chromosomes at late prophase I, with relatively few
292 clear examples of well separated bivalents (compare Fig. 4G to 4H-I). The tendency

293 and degree of aggregation varied in the mutant plants, even for cells from the same
294 anther. The majority of the mutant cells showed these late prophase I phenotypes.
295 This late prophase I clumping phenotype is intriguing given that telomere-NE tethering
296 normally persists even after the bouquet stage. These results place MLKS2 in the
297 poorly understood pathway that ensures uniform dispersal of bivalents after pachytene.
298 Anaphase and telophase can be particularly informative stages for detection of
299 abnormal chromosome segregation. We found that the *mlks2-2* mutants showed
300 numerous such segregation defects, including chromosomes not in the metaphase I
301 plate bundle (arrows, Fig 4L-N). The mutant plants frequently showed chromosome
302 laggards (Fig. 4P-Q) and micronuclei (Fig. 4R), both of which are indicative of
303 missegregation. Frequency of cells with one or more aberrant patterns at meiosis I
304 (metaphase, anaphase, telophase) were low for wild-type (5%, n = 200) but high for
305 *mlks2-2* (46%, n = 303) Specifically, the percentages of cells with abnormal
306 chromosomes per stage were 61% in diakinesis (n=109), 37% in metaphase I (n=123),
307 60% in anaphase I (n=10), and 34% in the combined stages of telophase I, telophase
308 II, and 4-nucleate tetrad (n=61).
309 We next checked for post-meiotic phenotypes associated with pollen viability.
310 Acid fuchsin and malachite green differential pollen staining revealed that both *mlks2-1*
311 and *mlks2-2* plants showed reduced pollen viability compared to normal plants (Fig. 4S-
312 V, n>1,000 for each genotype). The pollen sterility phenotype was only partially
313 penetrant and, like the other phenotypes, more severe for *mlks2-2*. Taken together,
314 these phenotypes show that MLKS2 is required for proper male reproduction, with
315 cytological phenotypes appearing as early as the zygotene bouquet stage of meiosis.

316

317 ***MLKS2* plays a conserved role in nuclear shape maintenance in root hair cells**

318 Root hair nuclei in plants are pleomorphic, and in Arabidopsis their shape and
319 positioning are disrupted by mutations in LINC or LINC-associated genes (Dittmer and
320 Richards, 2008; Oda and Fukuda, 2011; Tamura et al., 2013; Zhou et al., 2012).
321 Interestingly, this rounding up or loss of elongation nuclear shape phenotype appears to
322 be generally diagnostic for genetic disruption of the LINC complex. We measured
323 nucleus lengths in maize root hairs 5 days after imbibition, from normal and *mlks2*
324 mutants. Normal (W22, also designated W22+ or wild-type) nuclei averaged a length of
325 37 microns, but mutant nuclei were only half that long on average (Fig. 5A, B). A
326 related measure, circularity index from edge-traced nuclei in 2D images, also changed
327 from 0.4 in normal plants to a more circular value of 0.7 in the more "rounded up"
328 mutants (Fig. 5C). Although the biological role of root hair nuclear elongation remains
329 to be determined, these shape measures provide a quick and quantitative phenotypic
330 readout for genetic disruption of the LINC complex at the seedling stage.

331

332 ***MLKS2* is required for normal stomatal complex development**

333 While screening seedling leaf tissues for nuclear shape phenotypes, we found an
334 unexpected and dramatic effect on stomatal complex development in*mlks2* mutants, as
335 summarized in Figure 6. Normal stomatal development in maize leaves (reviewed by
336 Smith, 2001) results in a bilaterally symmetric 4-cell complex composed of 2 dumbbell-
337 shaped guard cells (GC in Fig. 6A) flanked by two subsidiary cells (SC in Fig. 6A). In
338 the *mlks2* mutants, the subsidiary cells, but not the guard cells, exhibited dramatic and

339 variable deviations (denoted by arrows, Fig. 6D-I) in size, shape, and number per
340 stomatal complex. Given the known role of asymmetric cell division in the normal
341 development of the guard cell complex, we checked for cell polarity phenotypes at
342 earlier stages of development. Images from the meristematic base of the fourth leaf
343 showed that the *mlks2-2* mutant exhibited irregular cell polarities and division planes
344 (Fig. 6L), abnormal shaped subsidiary cells (Fig. 6O), or extra inter-stomatal and
345 subsidiary mother cells (Fig. 6K, N). These phenotypes closely resemble those of the
346 *pangloss* or *brick* mutants of maize, known to perturb nuclear positioning and the actin
347 cytoskeleton, culminating in irregular subsidiary cell development. These findings
348 uncover an unanticipated developmental role for *MLKS2* that likely reflects its function in
349 cell polarization and nuclear positioning for specialized, highly asymmetric cell divisions
350 leading to the differentiation of the stomatal complex.
351

352 **MLKS2 interacts with F-actin via its ARM domain and is required for recruitment**
353 **of meiotic perinuclear actin**

354 Given that MLKS2 has ARM domains, localizes to a cytoskeletal-like network,
355 and shows mutant phenotypes suggestive of cytoskeletal interactions, we wanted to
356 more directly explore the interaction of MLKS2 with actin. First, GFP-MLKS2 was co-
357 expressed with markers for the endoplasmic reticulum (RFP-HDEL), the actin
358 cytoskeleton (RFP-Lifeact) or the microtubule cytoskeleton (mCherry-TUA5) as shown
359 in Figures 7, S2. Colocalization of GFP-MLKS2 was seen for both ER and F-actin but
360 not microtubule markers (Fig. 7A, S2). The actin, but not the ER colocalization with
361 MLKS2, requires the presence of the MLKS2 ARM domain region (Fig. 7B). To further

362 characterize the interaction of MLKS2 with F-actin, we examined the localization of
363 MLKS2 in cells treated with Latrunculin-B (LatB) to depolymerize the F-actin. This
364 treatment caused the GFP-MLKS2 staining pattern to change from fibrous to a more
365 ER-like network, similar to that of the ARM domain deletion of MLKS2 (compare 2B to
366 7C). These findings show that when expressed in tobacco, MLKS2 appears to induce
367 an actin-ER colocalization. MLKS2 appears to connect the ER to F-actin through its
368 ARM domain. Consistent with this, the mobile fraction of MLKS2 in the NE was
369 increased after F-actin depletion by LatB (Fig. 7D, E). This result provides additional
370 evidence that MLKS2 binds to F-actin in an ARM domain-dependent manner.
371 Given these results together with the previously established roles for some KASH
372 proteins' actin-based nuclear anchoring (Gundersen and Worman, 2013; Huelsmann
373 and Brown, 2014; Zhou et al., 2014), we next asked if GFP-MLKS2 could affect nuclear
374 mobility in a live cell assay. The nuclear mobility baseline was first established in
375 *N. benthamiana* using GFP-LBR (Graumann et al., 2010) as a general NE marker (Fig.
376 7F-H). For these experiments, nuclear movement was tracked in live cells for five min
377 by imaging at 10 s intervals to obtain total distance migrated. Compared to the GFP-
378 LBR-expressing control, the nuclei expressing GFP-MLKS2 were dramatically
379 immobilized as shown by temporal color-coded projections, kymograph analysis (Fig.
380 7F-G), and measurements of total distance of nuclear movement over the 30-frame
381 time-lapse (Fig. 7H). Expression of MLKS2 and MLKS2ΔKASH resulted in significant
382 decreases in nuclear movement compared to the LBR control. In contrast, the nuclear
383 anchoring activity of MLKS2 could be abolished by deletion of the ARM domains (Fig.
384 7H). These live nuclear mobility assays define an ARM-dependent nuclear anchoring

385 activity for MLKS2, consistent with the core function of the LINC complex in connecting
386 the nucleus to the cytoskeleton.
387 Given the role of the NE dynamics in meiotic prophase and our findings that
388 MLKS2 interacts with F-actin in somatic cells, we returned to maize to check genetic
389 evidence of MLKS2-actin interactions in pollen mother cells at meiotic prophase (Fig. 7I-
390 P). The overall appearance of phalloidin-stained F-actin in W22 was similar to that of
391 *mlks2-2* meiocytes, with two notable exceptions. First, the F-actin in the mutant plants
392 appeared to exhibit a subtle phenotype of somewhat discontinuous or fragmented F-
393 actin structures (compare fiber lengths of Fig. 7 panels J and L versus N and P).
394 Secondly, and most importantly, we observed that the *mlks2-2* meiocytes exhibited a
395 conspicuous loss of perinuclear F-actin staining. Perinuclear actin is common in maize
396 meiocytes (Murphy et al., 2014) and intensity line profile tracings show clear evidence of
397 F-actin concentration spikes around the nucleus (yellow arrows, Fig. 7M, N). However,
398 we were unable to observe by inspection (Fig. 7I-L) or line profile analysis (Fig. 7M-P)
399 any such perinuclear actin staining in *mlks2-2* mutant meiocytes. These findings
400 implicate MLKS2 in the formation of perinuclear F-actin to achieve proper meiotic
401 chromosome behavior.
402
403 **MLKS2 can rescue Arabidopsis triple *wip* nuclear shape phenotype**
404 Finally, the functional conservation of MLKS2 in plants was addressed using a
405 genetic rescue assay. Previously, it has been shown that deletion of certain KASH
406 proteins, such as AtWIP proteins, causes nuclei to become more circular (Zhou et al.,
407 2012). GFP-MLKS2 was expressed in Arabidopsis harboring mutations in three *WIP*

408 genes to determine if the maize SINE-group KASH protein could correct the nuclear
409 shape defect phenotype. For this experiment, stable transformants expressing GFP-
410 MLKS2 were grown and nuclei were imaged and analyzed from two different tissues, as
411 shown in Figure 8. Circularity index measurements of leaf and root nuclei showed that
412 maize GFP-MLKS2 complemented the nuclear shape phenotype of the triple-*WIP*
413 mutant in Arabidopsis by restoring the nuclei to wild-type length in two different cell
414 types. These experiments demonstrate that a GFP-tagged maize SINE-family KASH
415 protein can substitute for Arabidopsis *WIP*-family KASH proteins in nuclear shape
416 control. In summary, the findings from this study establish that the maize KASH protein
417 MLKS2 plays a role in multiple biological pathways including stomatal complex
418 development, meiotic nuclear architecture and positioning, meiotic chromosome
419 segregation, and production of viable pollen.
420

421 ## Discussion

422 In this study we characterized a core LINC component, MLKS2, in maize using
423 genetic and cellular assays. We showed that MLKS2 localizes to two cellular
424 compartments, the NE as expected and cytoplasmic ER where it colocalizes with actin
425 via the ARM domain region. Genetic analysis uncovered mutant phenotypes in both
426 vegetative and reproductive organs while documenting the first case of a plant KASH
427 required for proper telomere clustering and chromosome behavior in meiotic prophase.
428 Interactions of MLKS2 with F-actin via the ARM domains of MLKS2 may represent a
429 general mechanistic principle that explains how MLKS2 might control nuclear shape and
430 positioning. The pleiotropic nature of the mutants and MLKS2's deep conservation in
431 plants may be important for a variety of tissue-specific biological functions that require
432 specialized control of nuclear morphology and dynamics. For instance, MLKS2 may
433 play a role in female meiosis and ovule development where highly organized nuclear
434 positioning occurs in the mature ovary, pollen development and nuclear migration of
435 sperm and vegetative nuclei, and fertilization itself. Interestingly, the overall plant
436 morphology of both the wild type (WT) and homozygous mutant plants was largely
437 normal.

438 At the onset of this study, the diagnostic ARM domains of the SINE group of
439 plant KASH and previous findings from Arabidopsis AtSINE1 (Zhou et al., 2014) pointed
440 to a possible MLKS2 interaction with F-actin. Interestingly, GFP-AtSINE1, but not GFP-
441 AtSINE2, colocalizes with F-actin when expressed in tobacco or Arabidopsis (Zhou et
442 al., 2014). Medicago SINE-group KASH genes, *MtSINE1* and *MtSINE2*, also encode
443 proteins that colocalize with F-actin (Newman-Griffis et al., 2019). The ARM domains

444 alone may not, therefore, be predictive of F-actin binding. Consistent with this is the fact
445 that a variety of proteins have ARM domains, but their binding partners vary (Coates,
446 2003). In this study, there exists a clear preponderance of evidence, direct and
447 indirect, that MLKS2 has F-actin binding activities. In the heterologous expression
448 system, MLKS2 localizes to the NE, as expected for a KASH domain protein, and to a
449 cytoskeletal-like reticulate network that colocalizes with F-actin and ER markers at the
450 cell periphery (Fig. 7A). Two complementary cell localization experiments, latrunculin-B
451 depletion of F-actin and ARM domain deletions, uncover a possible cytoplasmic function
452 that does not involve the nucleus, but rather deploys MLKS2 to tether the ER to
453 cytoplasmic F-actin. In this regard, MLKS2 resembles members of the Networked
454 (NET) proteins, as defined by Hussey and colleagues (Deeks et al., 2012). Although
455 MLKS2 does appear to fit the definition of membrane-bound plant-specific actin-binding
456 adapter protein, it lacks the tryptophan-rich NET actin-binding (NAB) domain sequence,
457 common to NET families 1-4 (Hawkins et al., 2014). The NET NAB domain is thought
458 to confer actin-binding activity, whereas for MLKS2 that activity may come from the
459 ARM domain. We note that the non-nuclear cytoplasmic MLKS2 may result from
460 overexpression or compromised targeting in the heterologous expression system used.
461 It nonetheless predicts that misregulation by overexpression may present cellular
462 dysfunction phenotypes generally associated with the cytoplasm and specifically
463 associated with the ER and cortical F-actin.
464 The actin interaction with core LINC NE components provides mechanistic
465 insights into several cellular functions of MLKS2 in both vegetative and reproductive
466 parts of the maize plant. We focused on three major nuclear phenotypes assayed

467 primarily in somatic cells: (1) positioning within the cell, (2) shape, and (3) mobility.
468 Nuclear positioning was implicated by genetic analysis of stomatal complex
469 development, nuclear shape was examined via rescue of root hair nuclei rounding up,
470 and nuclear mobility was directly measured in live cells.

471 Nuclear positioning defines cell polarity. One well-characterized example of
472 highly polarized cells associated with asymmetric cell divisions is the normal stomatal
473 complex development in leaves. In wild-type maize, guard mother cells (GMC) signal to
474 adjacent subsidiary mother cells (SMC) to commence a series of cellular events
475 involving nuclear migrations and localized actin patches that coordinate the eventual
476 production of a mature stomatal complex (Müller et al., 2009). The mature stomatal
477 complex is characterized by two guard cells flanked by subsidiary cells, displaying a
478 bilateral symmetry. Mutations known to disrupt stomatal complex development in maize
479 include the *discordia* (*dcd1*), the *panglass* (*pan1*, *pan2*), and the *brick* (*brk1*, *brk2*, and
480 *brk3*) mutants (Facette et al., 2015). The brick proteins are part of the SCAR complex
481 which interacts with ARP to form actin patches on the GMC side of the SMC. How the
482 nucleus moves towards the actin patches is not known. The KASH phenotypes
483 reported here bear a striking resemblance to those of *pan1* and *brk1*, placing *MLKS2* in
484 the stomatal complex development pathway. Given that MLKS2 ARM domains appear
485 to interact with F-actin, it is tempting to speculate that the developmental defect seen in
486 *mlks2* reflects a failure to coordinate nuclear positioning with the cortical-ER-patches
487 known to occur at the region adjacent to the inducing GMC (Giannoutsou et al., 2011).

488 Nuclear shape maintenance is one of the fundamental functions performed by
489 LINC complex proteins. Nuclear morphology is commonly altered in LINC mutants,

490 some of which present pathological conditions such as envelopathies (Burke and
491 Stewart, 2006; Janin et al., 2017). In eudicot plants, disruption of LINC components
492 cause alterations in root hair nuclear shape phenotypes (Newman-Griffis et al., 2019;
493 Oda and Fukuda, 2011; Tamura et al., 2013; Zhou et al., 2015a). In maize, we similarly
494 observed that *mlks2* nuclei change to more compact and spherical shapes than those
495 from normal cells (Fig. 5A-C). There is growing evidence that disruption of any
496 component of the core LINC components or even the LINC-interacting nucleoskeletal
497 proteins can cause a "rounded up" nuclear phenotype. The finding that maize GFP-
498 MLKS2 was able to rescue the nuclear shape phenotype in Arabidopsis plants lacking
499 three WIP proteins is important for two reasons. First, it represents the first
500 demonstration of cross-species genetic rescue of a LINC component. Second, it
501 suggests that even diverged LINC components may possess some degree of structural
502 redundancy in establishing a balance of forces required for maintaining nuclear shape.
503 The triple *WIP* rescue by a maize SINE-group KASH may reflect, therefore, the capacity
504 of MLKS2 to replace a NE-cytoskeletal tether normally formed by the WIP--WIT--
505 MyosinXI-i-actin bridge (Tamura et al., 2013).
506 Nuclear mobility in plants is associated with a wide variety of cellular processes
507 including symbiosis, pathogenesis, fertilization, and division planes in development
508 (Griffis et al., 2014). Nuclear mobility can either be inferred from variable positioning in
509 fixed cells, such as the eccentric nucleus stage of early meiotic prophase (Fig. 4), or by
510 direct time-lapse tracking in live cells (Fig. 7F-H). Here we observed both. Our results
511 show that the mobility of tobacco nuclei is reduced or stopped by heterologous
512 expression of GFP-MLKS2, and this immobilization is reversed by removing the ARM

513 domain region of MLKS2. These findings, consistent with our genetic analyses,
514 implicate MLKS2 in nuclear anchoring, which may further explain, for example, the
515 appearance of wild-type elongated nuclei in root hair cells (Fig. 5). The lack of
516 perinuclear actin around the meiotic nucleus in *mlks2-2* plants further suggests that
517 MLKS2 may function to bind or recruit filamentous actin to the perinuclear cytoplasm. In
518 this way, MLKS2 may play an organizational or mechanical role whereby
519 microfilaments, microtubules, or their associated motor proteins may direct the
520 dynamics of meiotic nuclei (Sheehan and Pawlowski, 2009).

521 The role of the NE in meiotic chromosome behavior has been recognized for
522 over a century. In recent decades, the LINC complex has been shown to be required for
523 telomere clustering at the bouquet stage, as first described in fission yeast (Chikashige
524 et al., 2009). Here we show that MLKS2 is required for normal bouquet formation and
525 proper chromosome segregation. Our findings represent the first genetic evidence that
526 a plant KASH interacts with the actin cytoskeleton during male meiosis. These results
527 suggest that actin may be more important in plant meiosis than previously recognized.
528 This idea is consistent with live imaging of maize meiotic prophase chromosome and
529 nuclear movements, both of which were stopped following MF depletion by latrunculin-B
530 treatment (Sheehan and Pawlowski, 2009). In our mutants, the earliest cytological
531 meiotic defect is seen at the zygotene stage, when the telomere bouquet is normally
532 formed. The *mlks2* mutants exhibit defects in telomere clustering and nuclear
533 positioning. These early stage problems may later manifest in the failure of homologs to
534 synapse and recombine with high fidelity. MLKS2 may also have post-bouquet
535 functions such as interlock resolution and telomere dispersal, ideas consistent with

536 detection of irregular and pronounced clumping at late prophase (Fig. 4G-J). The
537 chromosome segregation laggards, micronuclei, and pollen sterility phenotypes may
538 therefore reflect multiple upstream failures of disomic pairing and recombination.
539 Interestingly, several of our *mlks2* phenotypes resemble those described for mutations
540 in AtSUN genes (Varas et al., 2015) or the meiotic kinesin1-like gene *AtPSS1 (Duroc et*
541 *al., 2014)*. *AtSUN1-1* and *AtSUN2* double mutants also show partial polarization of
542 telomeres, absence of full synapsis, presence of unresolved interlock-like structures,
543 and reduction in the mean cell chiasma frequency which manifests in the formation of
544 laggard chromosomes during anaphase and severely reduced fertility (Varas et al
545 2015). Several of these phenotypes are the same or similar to what we observed with
546 *mlks2*, which is not surprising given that SUN and KASH are core components of the
547 LINC complex. Similarly, mutations in *AtPSS1* leads to phenotypes shared with mlks2,
548 including production of univalents and aneuploid cells after meiosis (Duroc et al 2014).
549 Findings such as these, together with the large body of evidence implicating
550 microtubules in plant meiotic chromosome behavior (Cowan and Cande, 2002; Cowan
551 et al., 2002; Driscoll and Darvey, 1970; Higgins et al., 2016; Shamina, 2003; Thomas
552 and Kaltsikes, 1977) suggest that meiotic chromosome behavior likely requires both
553 actin and tubulin cytoskeletal systems. Indeed, the LINC complex in general, and
554 MLKS2 in particular, may provide a coordinating structure that integrates cytoskeletal
555 systems to affect nuclear architecture.
556 In conclusion, this study identifies MLKS2 as a core LINC component with
557 multiple functions in fundamental plant vegetative and reproductive processes. Analysis
558 of the ARM domain sheds light on how the SINE group of plant KASH proteins can

559 interact with the actin cytoskeleton. In Figure 9, we present a working model for MLKS2
560 where we propose that MLKS2 interacts with F-actin via its N-terminal ARM domains in
561 wild-type (Fig. 9A) but not mutant plants (Fig. 9B). The MLKS2 protein could extend a
562 Velcro-type hook into the cytoplasm to bind generally or specifically with cytoskeletal
563 linear polymers, most likely F-actin. This interaction between MLKS2 and F-actin could
564 be achieved by direct or indirect contact (Fig. 9B, compare left and right). In tobacco
565 (Fig. 9C,D), the expression of GFP-MLKS2 or GFP-MLKS2ΔKASH results in nuclear
566 anchorage according to kymograph analysis, suggesting the ARM domain can anchor
567 the nucleus even if the KASH domain is absent. The anchorage is relieved by removal
568 of the ARM domains (Fig. 9D, right half). The models based on heterologous
569 expression in *N. benthamiana* include GFP-MLKS2 in the core LINC complex via a
570 presumed interaction with tobacco SUN (NbSUN, grey), or a demonstrated interaction
571 with maize SUN2 (red, ZmSUN2). These findings highlight the importance of
572 investigating individual components of the LINC complex in order to understand how the
573 NE coordinates cytoplasmic and nuclear phenomena to carry out fundamental biological
574 processes at the cellular level.
575
576

577 ## Materials and Methods:

578

579 **Microscopy with tobacco and Arabidopsis**

580 *Nicotiana benthamiana* (*Nb*) transformation was performed as described (Sparkes et al.,
581 2006). Agrobacterium cultures were used at an OD of 0.05 and plants imaged 3 days

post-infiltration. All imaging was performed on a Zeiss LSM 800 confocal system equipped with a 100X 1.4NA lens. Bi-directional scanning was used for all imaging. For DAPI excitation the 405nm laser was used and emission collected at 400-491 nm. For GFP excitation the 488 nm laser was used and emission collected between 491-617 nm. For mCherry excitation the 561 nm laser was used and emission collected from 561-620 nm. Colocalization imaging was performed with multi-track line switching to avoid fluorescence bleedthrough, and 4x frame averaging was used. For FRAP acquisition a 5X digital zoom was used with a frame time of 0.15s. Fluorescence recovery was monitored by consecutive imaging of 240 frames. Bleaching was performed after 5 control frames were imaged using the 488 nm laser at 100X power for 20 iterations in a 160x160 pixel ROI containing the NE. For nuclear movement assays, nuclei were imaged at 10 s intervals for 30 frames (5 minutes). We used LBR-GFP as a control for baseline nuclear movement as described in (Graumann et al., 2010). For DAPI staining, *N. benthamiana* or *A. thaliana* tissue was incubated in 5µg/ml DAPI and 0.001% Triton X-100 for 10 min before imaging.

For image analysis *ZEN* (Blue edition, v2.3.69.1000, Zeiss) was used and figures compiled in *Illustrator* (v22.1, Adobe). For FRAP analysis, normalized intensity values were calculated as described (Martinière et al., 2012), and one-phase association for each replicate and combined curves plotted in *GraphPad* v7.04. For nuclear movement assays, manual tracking was used to track the center of nuclear movement for each experimental condition, and FIJI (Image J version 1.52h) was used to generate temporal color-coded projections and kymographs over a 25 µm line. All whisker plots showing data points were generated in *GraphPad* v7.04. Student's T-test or one-way ANOVA

605 statistical tests were used depending on the suitability of the data, as indicated in each
606 figure legend. The number of replicates used for each experiment can be found in the
607 figure legends. Circularity index analysis was performed as described (Zhou et al.,
608 2012).
609
610 **Gene constructs**
611 Gene constructs, nomenclature, and sequence information for the clones used in this
612 study are listed in Table S1. GFP-MLKS2 constructs were synthesized (GenScript
613 Biotech Corp.) using the full-length ORF of MLKS2 fused to the C-terminal end of
614 eGFP-FLAG-HA. The synthetic clone (GFP-MLKS2) was obtained in a pUC18 vector,
615 inserted at the *Bam*HI restriction site to produce a plasmid designated pHWBF07. From
616 this vector, the eGFP-FLAG-HA-MLKS2 sequence was PCR amplified with *att* flanking
617 primers (Table S2) using high fidelity Q5 polymerase (NEB) and cloned into pDONR221
618 vector by BP cloning (Cat. No. 1235019, Invitrogen) to generate the entry clone
619 designated pHWBF07EC. The eGFP-FLAG-HA-MLKS2 sequence from the entry clone
620 was transferred to vector pH7WG2 (Karimi et al., 2002) by Gateway LR recombination
621 (Cat. No. 1235019, Invitrogen) to obtain the expression vector designated pPK1Fexp.
622 Deletion constructs were generated from the full-length entry clone as a template to
623 PCR-amplify required regions with internal primers containing flanking *att* sequences
624 and cloned into pDONR211 by Gateway BP cloning method. These deletion constructs
625 were also subcloned into pH7WG2 destination vector by Gateway LR recombination.
626 Full length and domain deletion constructs for ZmSUN2 were generated as described in
627 (Gumber et al., 2019).

628

629 **Maize plant material and genotyping**

630 The transposon insertion alleles of *MLKS2* (unique insertion IDs: mu1038603 and
631 mu1058535) were identified through MaizeGDB (http://www.maizegdb.org/) and derived
632 from the UniformMu transposon mutagenesis project (McCarty and Meeley, 2009;
633 Settles et al., 2007). Seeds for stock number UF-Mu04133 carrying allele *mlks2-1* or
634 stock number UF-Mu07312 carrying allele *mlks2-2* were obtained from the Maize
635 Genetics Cooperation Stock Center (http://maizecoop.cropsci.uiuc.edu/). For "wild-
636 type" maize referred to here as W22, we used color-converted W22 obtained from Hugo
637 Dooner (Waksman Inst., Rutgers, New Jersey, USA) derived by Brink (Brink, 1956).
638 The seeds were planted at the Florida State University Mission Road Research Facility
639 (Tallahassee, FL, USA) and propagated by out-crossing to W22 in summer 2014. In the
640 fall, the progeny seeds were grown in a greenhouse in the King Life Sciences building
641 (Biological Science Dept, Florida State University, Tallahassee, FL). The segregating
642 outcross plants were self-crossed to obtain mutant plants from among the progeny.

643 For PCR genotyping, leaf samples from 4-week-old maize W22 and plants from
644 families segregating for MLKS2 alleles were harvested, frozen, and stored at -80 C.
645 Genomic DNA was isolated using a modified mini-CTAB method from approximately 2
646 cm^2 leaf tissue in 96 well plates in a Mixer Mill (Retsch®) as described (Labonne et al.,
647 2013). Plants were genotyped using three different primer pair combinations to
648 accurately predict the genotype as described by (McCarty et al., 2013). For the *-mlks2-1*
649 allele, DNA extracted from each of the UF-Mu04133 stock plants was individually
650 amplified with 603F1-603R1 gene specific primer pair, as well as a gene specific primer

651 in combination with the Tir6 primer corresponding to terminal inverted repeats of the
652 Mu1 transposable element (603F1-Tir6 and 603R1-Tir6). Similarly, for the *mlks2-2*
653 allele, DNA extracted from each of the UF-Mu07312 stock plants was individually
654 amplified with 535F2-535R2, 535F2-Tir6 and 535R2-Tir6 primer pairs. Normal W22
655 DNA was also amplified with all of these primer pairs. All the primer sequences used for
656 genotyping are listed in Table S3. The PCR amplification products were resolved by
657 agarose gel electrophoresis followed by ethidium bromide staining. The PCR products
658 were sequence-verified using TA cloning in pCR™4Blunt-TOPO® Vector (Invitrogen cat
659 # K2875-20). M13F and M13R vector primers were used for sequencing (Molecular
660 Cloning Facility, Department of Biological Sciences, Florida State University) and the
661 resulting sequences were aligned with the W22 reference genome sequence to validate
662 the mu transposon element insertion sites.
663
664 **RNA extraction and qRT-PCR**
665 After one round of outcrossing to W22 and two rounds of self crossing, seeds were
666 grown in the greenhouse to harvest meiotic tassels from V13 -stage plants. The tassels
667 were frozen in liquid nitrogen and stored at -80°C until further use. The tissue was
668 ground in liquid nitrogen and 100 mg of the resulting powder used for RNA extraction as
669 per manufacturer's instructions (Qiagen RNeasy kit, Cat # 74904). The extracted RNA
670 was treated with amplification-grade DNase I (ThermoFisher, Cat # 18068015) for 15
671 min at room temperature, then treated with RNA clean and concentrator-25 kit (Zymo
672 Research, Cat # R1017). The resulting RNA was inspected for quantity and quality by
673 UV spectroscopy and gel electrophoresis, respectively. Superscript III reverse

674 transcriptase (ThermoFisher, Cat# 18080093) was used to reverse transcribe 1μg of
675 high quality RNA into cDNA according to the manufacturer's instructions. The resulting
676 cDNA was used as a template to amplify ~ 100 bp products downstream of Mu1
677 insertion sites in *mlks2-1* and *mlks2-2* using three gene-specific primers. Two
678 housekeeping genes CDK1 and RPN2 were amplified as internal controls (Lin et al.,
679 2014). The products were amplified using SYBR Green Master Mix (Applied
680 Biosystems) on a 7500 Fast Real-Time PCR System (Applied Biosystems). Relative
681 expression change was calculated using the 2ΔΔCt method (Livak and Schmittgen,
682 2001). Two technical replicates were carried out to ascertain the accuracy of the
683 procedure.
684
685 **Microscopy in maize**
686 For 3D telomere FISH analysis, meiotic stage tassels were harvested from W22
687 and *mlks2-2* plants grown in the greenhouse. Flowers were microdissected and fixed in
688 1X Buffer A with 4% paraformaldehyde for 1 hour on rotary shaker at room temperature
689 as described (Bass et al., 1997). The fixed anthers were microdissected and embedded
690 in acrylamide pads as described in (Howe et al., 2013) and subjected to telomere FISH
691 using a 0.13 μM fluorescein-conjugated telomere-specific oligonucleotide probe, MTLF.
692 The meiocytes were counterstained with 3 μg/mL DAPI then mounted in vectashield
693 (Vector labs) and imaged using a 3D-deconvolution microscope equipped with a 60X
694 lens and CCD camera (Deltavision, GE Healthcare). Telomere coordinates in X, Y, and
695 Z were identified using the 3D MODEL tool of SoftWorx program (DeltaVision, GE

696 Healthcare) and pairwise telomere distances were calculated using R software for
697 Euclidean distances.
698 For actin staining, meiotic-staged anthers were fixed in PHEMS buffer
699 supplemented with 8% paraformaldehyde for 2 hours with shaking at room temperature
700 as described (Chan and Zacheus Cande, 1998). The fixed anthers were microdissected
701 on a glass slide in PBS (pH 7.0) and stained with 3.3 µM Alexa Fluor™ 594 Phalloidin
702 (Thermo Fisher Scientific) and DAPI (1.5 µg/mL) for 20 min at room temperature in the
703 dark. The cells were imaged using a Deltavision 3D deconvolution microscope.
704 For pollen viability, anthers from male flowers just before dehiscence were fixed
705 in Carnoy's fixative (6 alcohol:3 chloroform:1 acetic acid) for a minimum of 2 hours at
706 room temperature. The fixed anthers were placed on glass slides and stained with
707 modified Alexander's stain containing Malachite green (0.01%), Acid Fuchsin (0.05%)
708 and Orange G (0.005%) as described (Peterson et al., 2010) to differentiate viable
709 (magenta) pollen grains from aborted (green) pollen grains. Bright field images of pollen
710 grains were collected on Revolve microscope (Echo Labs). At least 300 pollen grains
711 each from 3 plants of every genotype were counted to calculate pollen viability.
712 For maize root hair imaging, seeds were sterilized with 1% bleach, 0.01% Triton
713 X-100 in deionized water for 10 min, rinsed and soaked in water overnight. The next
714 day seeds were spread on wet paper towels, kept dark and moist for 5-6 days, then
715 roots were cut off and fixed in Buffer A (Howe et al., 2013) plus 4% final concentration
716 paraformaldehyde for 1 hour, with rotation at room temperature. Small pieces of roots
717 with root hair from the elongation zone were placed on glass slides and chopped to
718 small pieces with a razor blade. The tissue was stained with 3 µg/mL DAPI for 20 min

719 at room temperature, mounted with VECTASHIELD, and imaged on an EVOS
720 fluorescence microscope (Thermo Fisher Scientific). The images were processed using
721 the *Analyze particle* function of *ImageJ* to measure the longest diameter and circularity
722 of the nuclei.

723 For leaf and stomatal complex imaging, plants were grown in the greenhouse
724 and the 4th leaf was harvested at its first appearance. For developing stomatal complex,
725 up to 2 cm tissue from the base of the leaf was harvested, and for mature stomatal
726 complex, the remainder of the leaf was harvested and fixed in FAA fixative (3.7%, 10%
727 Formalin, 50% ethanol and 5% acetic acid in water) for at least 15 min at room
728 temperature as described in (Facette et al., 2015). The leaf tissue was cut in thin
729 longitudinal strips and treated with PBS supplemented with 1% Triton for 10 min to
730 permeabilize the tissue. The tissue was then rinsed and incubated in a solution of
731 propidium iodide (Life technologies) and DAPI for 30 min. The tissue was rinsed with
732 PBS to get rid for excess dye and mounted in water. The tissue was imaged on a 3D
733 deconvolution microscope at 60X magnification.

734

735 ## Figure Legends

736

737 **Figure 1: Gene model and protein domain diagram of *MLKS2*.**

738 A) Gene model diagram for *MLKS2* with gene features drawn to scale. Total length of
739 the primary transcript (transcript model for B73v4 is indicated above) is 3007 bp. Three
740 exons are shown as black boxes. The 5'UTR of the gene is interrupted by "Intron 1."
741 Gene features are indicated: TSS, transcription start site; UTR, untranslated region;

742 ORF, open reading frame. B) The amino acid sequence of MLKS2 with domains
743 underlined with lines of different styles, or boxed. The protein sequence is identical to
744 that from genotype W22 (not shown) used for transposon mutagenesis. The key is
745 given under the sequence. C) Domain diagram for MLKS2 showing the names and
746 locations of secondary structural features (alpha helices) or domains are indicated. The
747 conserved terminal four amino residues (LVPT) at the end of the KASH domain are
748 shown . D) The I-TASSER protein structure prediction software was used with MLKS2
749 as input sequence. The top-ranked structural homolog is shown for a predicted tertiary
750 structure of MLKS2 (1st panel) next to the known structure of PP2A structural subunit
751 (pdb 1b3uA, 2nd panel), followed by an overlay of the two (3rd panel). The rainbow
752 annotation denotes the protein polarity from the N-terminus (blue) to the C-terminus
753 (red). The transmembrane (TMD) and KASH domains of MLKS2 are annotated.
754
755 **Figure 2: MLKS2 cellular localization and ZmSUN2-interaction.**
756 Subcellular localization of full length and deletion mutants of GFP-MLKS2 in transiently
757 expressing *N. benthamiana* leaf cells as previously described (Gumber et al., 2019). A)
758 Domain deletion diagram of all constructs used showing the ARM domain (yellow),
759 disordered regions (blue), transmembrane domain (TM), KASH domain (purple),
760 terminal AA residues, and stop codon (*). B) Full length GFP-MLKS2 (green) and all but
761 one deletion mutant localize to the NE around DAPI-stained chromatin (magenta). GFP-
762 MLKS2ΔTM appears soluble and distributed throughout the nucleoplasm. A cell
763 periphery network-like pattern was observed for all constructs, with GFP-MLKS2ΔTM
764 appearing as soluble in the cytoplasm and GFP-MLKS2ΔARM appearing as associated

765 with the ER. C) Fluorescence recovery curve from MLKS2 FRAP alone or when co-
766 expressed with mCherry-ZmSUN2, mCherry-ZmSUN2ΔCC (without coiled coil domain),
767 or mCherry-ZmSUN2ΔSUN (without SUN domain). D) FRAP recovery plateau values
768 for fluorescence recovery curves shown in C). E) Fluorescence recovery curves
769 showing increased mobile fraction in the NE for KASH or ARM domain deletion variants
770 of GFP-MLKS2. F) FRAP recovery plateau values of MLKS2, MLKS2ΔKASH, and
771 MLKS2ΔARM shown in D). Scale bar denotes 10 µm. For whisker plots, blue lines
772 denote SD error bars, red lines denote mean. Nuclei (N = ≥30) imaged across three
773 experimental repeats per treatment. ANOVA statistical test used where Ns = P≥0.05, ***
774 = P≤0.001 and **** = P≤0.0001.
775
776 **Figure 3. Genotypic characterization of *MLKS2* alleles.** Two transposon-tagged
777 alleles of *MLKS2, mlks2-1* and *mlks2-2* are depicted. A) *MLKS2* gene model showing
778 the location of *Mu1* transposon insertion sites (triangles) for two alleles. The positions of
779 allele-specific primer pairs (gF1, gR1 and gF2, gR2) and Tir6 primer (T6) at the Mu1
780 transposon terminal inverted repeat sequence are marked with arrows. The positions of
781 primer pairs (qF1, qR1; qF2, qR2; or qF3, qR3) used for qRT-PCR are also marked with
782 arrows. The PCR products (21FR, 21FT, 21TR, 22FR, 22FT, and 22TF) used for
783 sequence verification, genotyping, and quantitative RT-PCR are indicated below the
784 gene model. B) Sequences aligned around the insertion site include the published
785 parental sequence (Springer et al., 2018), the wild-type allele from PCR products ("a"
786 and "d") from W22, and the mutator-flanking sequences from PCR products ("b","c", "e",
787 and "f") using one gene primer and one mutator-specific primer (T6). In both alleles, a

788 9-bp duplication (underlined) was detected. C) Agarose gels showing PCR products
789 amplified from W22 and plants from families segregating for *mlks2-1* (top gel) or *mlks2-*
790 *2* (bottom gel) allele. The PCR products were amplified using gene-specific primer pairs
791 (lanes/PCR products a, d) or primer pairs from one gene-specific primer and one
792 mutator (T6) primer (lanes/PCR products b, c, e, f). Plant genotypes are shown on the
793 top of the gels, primer pairs and band sizes are indicated on the right. The lanes "M"
794 contain 100 bp DNA marker fragments at the lengths indicated. D) Fold change in the
795 transcript levels of *MLKS2* in families segregating for *mlks2-1* or *mlks2-2*; homozygous
796 WT siblings (+/+) or homozygous mutant plants (-/-) were quantified relative to W22
797 using an average of 3 primer pairs (qF1-qR1, qF2-qR2, qF3-qR3) as measured by qRT-
798 PCR.
799
800 **Figure 4: Multiple meiotic and post-meiotic defects of *mlks2* mutants.**
801 Cytological defects of *mlks2-2* during and after male meiosis. A) Early prophase I stage
802 W22 meiocyte nucleus showing a typical bouquet (green dots, "bq") of NE-associated
803 telomeres visualized in the nucleus (DAPI, shown in magenta) using the 3D acrylamide
804 oligo FISH method (Bass et al., 1997). B) Partial telomere bouquet in *mlks2-2* mutant at
805 meiotic prophase, showing unusually distant telomeres (arrows) relative to the main
806 bouquet (bq) telomere cluster region. C) Histogram showing bouquet-stage telomere
807 pairwise distance distributions plotted as log2 fold change of mutant/wild-type per 1
808 micron distance bins (n=6 W22, n=11 *mlks2-2*). The mutants show a pronounced
809 increase in the longer telomere-to-telomere distance bins. Nuclear position phenotypes
810 for normal D) or mutant E) cells shown as projections from the middle-most 1/5 of the

811 optical sections through the nuclei stained with DAPI, including traces around the cell
812 and nuclear peripheries to ascertain 2D centroid locations. F) Eccentricity plots
813 showing the distribution of distances of between the pairwise centroids of nuclei and
814 cells for normal (W22) and mutant (*mlks2*) meiocytes at at the bouquet stage, using the
815 same nuclei as those analyzed in A-C. G) Late prophase I stage W22 meiocyte showing
816 bivalents spread throughout the volume of the nucleus. H-J) Late prophase I stage
817 *mlks2-2* meiocytes showing clumping of bivalents. K) W22 meiocyte showing bivalents
818 on a normal meiosis I metaphase plate. L-N) Mutant *mlks2-2* meiocytes showing one or
819 more chromosomes (arrows) not located in the meiosis I metaphase plate. O) W22
820 meiocyte at late anaphase I or early telophase I. P-Q) Mutant *mlks2-2* late anaphase I
821 or early telophase I showing irregularly positioned "laggard" chromosomes (arrows). R)
822 Mutant mlks2-2 at telophase after meiosis I, before meiosis II, and showing micronuclei
823 (arrows) that are associated with failure of chromosomes or chromosomal fragments to
824 reach the spindle poles. S-U) Pollen viability stains for wild-type S) or mutant T, U)
825 pollen. Dark purple indicates viable pollen, light blue indicates inviable pollen. V)
826 Quantification of pollen viability with n=1,000 or more for each genotype.
827
828 **Figure 5. MLKS2 is required for the elongated nuclear shape phenotype in root**
829 **hair cells.**
830 A) Root hair nuclei stained with DAPI in W22, *mlks2-1* and *mlks2-2* maize plants. B)
831 Quantitation of longest dimension of W22, *mlks2-1*, or *mlks2-2* root hair nuclei. C)
832 Circularity index measurements of nuclei from W22, *mlks2-1* and *mlks2-2* in which 1.0
833 represents a perfectly round shape.

834

835 **Figure 6. MLKS2 is required for normal stomatal complex development.**

836 Mature stomatal complex in DAPI stained leaf from wild-type W22 (A-C), *mlks2-1* (D-F)
837 or *mlks2-2* (G-I) plants. For comparison, a typical stomatal complex has bilateral
838 symmetry with two elongated central dumbbell-shaped guard cells (GC) flanked by two
839 outer subsidiary cells (SC). In the *mlks2-1* D-F) or *mlks2-2* G-I) mutants, subsidiary
840 cells appear abnormal (arrows) in their number, shape, or nuclear position relative to
841 the guard cells. J-L) Representative images from early stages of stomatal development
842 where subsidiary mother cells (SMC) are polarizing, with nuclei migrating towards the
843 guard mother cells (GMC). Interstomatal cells (ISC) are annotated for W22. M-O)
844 Representative images of developing stomatal complex after SMC polarization.
845 Boundaries of abnormally shaped cells or cells with abnormal nuclear positioning are
846 marked with dotted lines. Scale bars denote 15 µm.

847

848 **Figure 7. MLKS2 interaction with actin.**

849 Co-localization of ER marker (RFP-HDEL, magenta) or actin marker (RFP-LifeAct,
850 magenta) with A) GFP-MLKS2 or B) GFP-MLKS2ΔARM. C) GFP-MLKS2 localization in
851 F-actin-depleted cells (25 uM LatB) phenocopies GFP-MLKS2ΔARM with an ER-like
852 staining pattern. D) Depolymerization of the actin cytoskeleton with LatB results in
853 increased GFP-MLKS2 FRAP recovery compared to mock (MK) controls. E) FRAP
854 Plateau value of MLKS2 mock (MK) and LatB treated as shown in D). For whisker plots,
855 blue lines denote SD error bars, red lines denote mean. Student's T-test used to test
856 statistical significance. **** = P≤0.0001. Scale bar denotes 10 µm. F) Temporal color-

857 coded projections of randomly selected LBR, MLKS2, MLKS2ΔKASH and
858 MLKS2ΔARM nuclei imaged every 10 seconds over 5 minutes. G) Kymographs of
859 nuclear movement shown in F) for a different nucleus. H) Quantification of total nuclear
860 movement over time, imaged for LBR, MLKS2, MLKS2ΔKASH and MLKS2ΔARM. N =
861 at least 30 nuclei imaged across three experimental repeats per treatment; ANOVA
862 statistical test used. Ns = P≥0.05, * = P≤0.05, *** = P≤0.001 and **** = P≤0.0001. (I-L)
863 DAPI (magenta) and phalloidin (green) stained early prophase maize meiocytes. (M-P)
864 Gray-scale images of phalloidin staining of cells shown in panels I-L. Line trace plots
865 show intensity of phalloidin in the middle of the cell marked by horizontal band,
866 illustrating the spike in perinuclear actin in wild-type but not mutant nuclei. Scale bar
867 denotes 15 μm.
868

869 **Figure 8. Arabidopsis triple *wip* mutant phenotype rescued with MLKS2.**

870 DAPI stained representative images of A) leaf and B) root nuclei from three
871 Arabidopsis genotypes: *Arabidopsis thaliana* WT (Col0); (Columbia WT strain), *wip123*
872 (*AtWIP*-type KASH triple mutant where *wip123* refers to genotype *wip1-1*, *wip2-1*, *wip3-*
873 *1*) (Zhou et al., 2015b), or *wip123* plus GFP-MLKS2 (WIP triple mutant transformed with
874 GFP-MLKS2). (C, D) Nuclear circularity index summaries for these same tissues and
875 genotypes are shown below each tissue/genotype combination, where 1 is a perfectly
876 round nucleus and values lower than 1 are a measure of nuclear elongation.
877 Arabidopsis WIP triple mutant nuclei are significantly more rounded (leaf CI=0.81±0.03;
878 root CI=0.72±0.02) than WT (leaf CI=0.56±0.03; root CI=0.39±0.02) whereas GFP-
879 MLKS2 complemented nuclei are similar to WT (leaf CI=0.52±0.03, root CI=0.32±0.02);

880 p>0.05=ns, p<0.0001=****.

881

882 **Figure 9. Summary diagrams and models of ZmMLKS2.**

883 Summary diagram illustrates how MLKS2 may interact with F-actin to produce the
884 genetic and heterologous expression phenotypes reported in this study. A) MLKS2 is
885 presumed to be arranged with an ARM domain-containing alpha solenoid structure in
886 the cytoplasm, where it interacts with F-actin directly (left half) or indirectly through a
887 hypothetical connector depicted by the boxed question mark (right half). B) The *mks2-2*
888 mutant has lost the ability to bind or contribute to the recruitment of F-actin. Not
889 depicted here are data from MLKS2 in vegetative (leaf, root) organs. Results from
890 kymograph analysis of GFP-MLKS2 expressed in *N. benthamiana* are summarized for
891 experiments that showed C) anchored nuclei in cells expressing full length MLKS2 or
892 MLKS2ΔKASH, or D) mobile nuclei in cells expressing a control NE marker (lbr) or
893 MLKSΔARM. In these diagrams, evidence for interaction with ZmSUN2 co-expression
894 is indicated (red) on the basis of FRAP assays or depicted from presumed interactions
895 with tobacco SUN, NbSUN (grey). In these diagrams (C,D), the MLKS2 interaction with
896 F-actin is depicted as direct for convenience, but the alternative indirect mode (A, right
897 half) of MLKS2 interaction with F-actin remains a formal possibility.

898

899 **Figure S1. Individual nucleus data from FRAP experiments presented throughout**
900 **the main figures**. A) FRAP recovery curves from all individual nuclei imaged with GFP-
901 MLKS2 for comparison to co-expression with SUN2. B) FRAP recovery curves from all
902 individual nuclei imaged with GFP-MLKS2 and co-expressing mCherry-SUN2. C) FRAP

903 recovery curves from all individual nuclei imaged with GFP-MLKS2 and co-expressing
904 mCherry-SUN2ΔCC. D) FRAP recovery curves from all individual nuclei imaged with
905 GFP-MLKS2 and co-expressing mCherry-SUN2ΔSUN. E) Halftime values from FRAP
906 recovery experiments shown in A-D. F) FRAP recovery curves from all individual nuclei
907 imaged with GFP-MLKS2 as control during GFP-MLKS2ΔKASH and GFP-
908 MLKS2ΔARM experiments. G) FRAP recovery curves from all individual nuclei imaged
909 with GFP-MLKS2ΔKASH. H) FRAP recovery curves from all individual nuclei imaged
910 with GFP-MLKS2ΔARM. I) Halftime values from FRAP recovery experiments shown in
911 F-H. J) FRAP recovery curves from all individual nuclei imaged with GFP-MLKS2 after 1
912 hour mock treatment, for comparison to LatB treatment. K) FRAP recovery curves from
913 all individual nuclei imaged with GFP-MLKS2 after 1 hour 25μM LatB treatment. L)
914 Halftime values from FRAP recovery experiments shown in J and K. Recovery curves
915 blue dots show individual data points, black lines individual fluorescence recovery
916 curves, and red curves average recovery curves for all nuclei. For whisker plots, blue
917 lines denote error bars showing standard deviation, red lines show mean values.
918 Statistical tests performed were either one-way ANOVA (E and I) or Student's t-test (L)
919 as appropriate. ns = P≥0.05, ** = P = ≤ 0.01.
920
921 **Figure S2. Co-expression of GFP-MLKS2 and tubulin alpha-5 (TUA5)**
922 Representative images of *N. benthamiana* leaves transiently co-transformed with GFP-
923 MLKS2 and mcherry-TUA5. MLKS2 and microtubules do not seem to colocalize. Scale
924 bar denotes 10 μm.
925

926 ## References

927

928 **Alam, S. G., Zhang, Q., Prasad, N., Li, Y., Chamala, S., Kuchibhotla, R., Kc, B.,**
929 **Aggarwal, V., Shrestha, S., Jones, A. L., et al.** (2016). The mammalian LINC
930 complex regulates genome transcriptional responses to substrate rigidity. *Sci. Rep.*
931 **6**, 38063.

932 **Barker, R. F., Thompson, D. V., Talbot, D. R., Swanson, J. and Bennetzen, J. L.**
933 (1984). Nucleotide sequence of the maize transposable element Mul. *Nucleic Acids*
934 *Res.* **12**, 6924–6924.

935 **Bass, H. W., Marshall, W. F., Sedat, J. W., Agard, D. A. and Cande, W. Z.** (1997).
936 Telomeres cluster de novo before the initiation of synapsis: a three-dimensional
937 spatial analysis of telomere positions before and during meiotic prophase. *J. Cell*
938 *Biol.* **137**, 5–18.

939 **Brink, R. A.** (1956). A Genetic Change Associated with the R Locus in Maize Which Is
940 Directed and Potentially Reversible. *Genetics* **41**, 872–889.

941 **Burke, B. and Roux, K. J.** (2009). Nuclei take a position: managing nuclear location.
942 *Dev. Cell* **17**, 587–597.

943 **Burke, B. and Stewart, C. L.** (2006). The laminopathies: the functional architecture of
944 the nucleus and its contribution to disease. *Annu. Rev. Genomics Hum. Genet.* **7**,
945 369–405.

946 **Chan, A. and Zacheus Cande, W.** (1998). Maize meiotic spindles assemble around
947 chromatin and do not require paired chromosomes. *J. Cell Sci.* **111**, 3507–3515.

948 **Chang, W., Worman, H. J. and Gundersen, G. G.** (2015). Accessorizing and
949 anchoring the LINC complex for multifunctionality. *J. Cell Biol.* **208**, 11–22.

950 **Chikashige, Y., Yamane, M., Okamasa, K., Tsutsumi, C., Kojidani, T., Sato, M.,**
951 **Haraguchi, T. and Hiraoka, Y.** (2009). Membrane proteins Bqt3 and -4 anchor
952 telomeres to the nuclear envelope to ensure chromosomal bouquet formation. *J.*
953 *Cell Biol.* **187**, 413–427.

954 **Coates, J. C.** (2003). Armadillo repeat proteins: beyond the animal kingdom. *Trends*
955 *Cell Biol.* **13**, 463–471.

956 **Cowan, C. R. and Cande, W. Z.** (2002). Meiotic telomere clustering is inhibited by
957 colchicine but does not require cytoplasmic microtubules. *J. Cell Sci.* **115**, 3747–
958 3756.

959 **Cowan, C. R., Carlton, P. M. and Cande, W. Z.** (2002). Reorganization and

960 polarization of the meiotic bouquet-stage cell can be uncoupled from telomere
961 clustering. *J. Cell Sci.* **115**, 3757–3766.

962 **D'Angelo, M. A.** (2018). Nuclear pore complexes as hubs for gene regulation. *Nucleus*
963 **9**, 142–148.

964 **Deeks, M. J., Calcutt, J. R., Ingle, E. K. S., Hawkins, T. J., Chapman, S.,**
965 **Richardson, A. C., Mentlak, D. A., Dixon, M. R., Cartwright, F., Smertenko, A.**
966 **P., et al.** (2012). A Superfamily of Actin-Binding Proteins at the Actin-Membrane
967 Nexus of Higher Plants. *Curr. Biol.* **22**, 1595–1600.

968 **Dittmer, T. A. and Richards, E. J.** (2008). Role of LINC proteins in plant nuclear
969 morphology. *Plant Signal. Behav.* **3**, 485–487.

970 **Driscoll, C. J. and Darvey, N. L.** (1970). Chromosome pairing: effect of colchicine on
971 an isochromosome. *Science* **169**, 290–291.

972 **Duroc, Y., Lemhemdi, A., Larchevêque, C., Hurel, A., Cuacos, M., Cromer, L.,**
973 **Horlow, C., Armstrong, S. J., Chelysheva, L. and Mercier, R.** (2014). The
974 kinesin AtPSS1 promotes synapsis and is required for proper crossover distribution
975 in meiosis. *PLoS Genet.* **10**, e1004674.

976 **Evans, D. E., Pawar, V., Smith, S. J. and Graumann, K.** (2014). Protein interactions at
977 the higher plant nuclear envelope: evidence for a linker of nucleoskeleton and
978 cytoskeleton complex. *Front. Plant Sci.* **5**, 183.

979 **Facette, M. R., Park, Y., Sutimantanapi, D., Luo, A., Cartwright, H. N., Yang, B.,**
980 **Bennett, E. J., Sylvester, A. W. and Smith, L. G.** (2015). The SCAR/WAVE
981 complex polarizes PAN receptors and promotes division asymmetry in maize. *Nat*
982 *Plants* **1**, 14024.

983 **Fernández-Álvarez, A., Bez, C., O'Toole, E. T., Morphew, M. and Cooper, J. P.**
984 (2016). Mitotic Nuclear Envelope Breakdown and Spindle Nucleation Are
985 Controlled by Interphase Contacts between Centromeres and the Nuclear
986 Envelope. *Dev. Cell* **39**, 544–559.

987 **Fournier, D., Palidwor, G. A., Shcherbinin, S., Szengel, A., Schaefer, M. H., Perez-**
988 **Iratxeta, C. and Andrade-Navarro, M. A.** (2013). Functional and genomic
989 analyses of alpha-solenoid proteins. *PLoS One* **8**, e79894.

990 **Giannoutsou, E. P., Apostolakos, P. and Galatis, B.** (2011). Actin filament-organized
991 local cortical endoplasmic reticulum aggregations in developing stomatal
992 complexes of grasses. *Protoplasma* **248**, 373–390.

993 **Godfray, H. C. J., Beddington, J. R., Crute, I. R., Haddad, L., Lawrence, D., Muir, J.**
994 **F., Pretty, J., Robinson, S., Thomas, S. M. and Toulmin, C.** (2010). Food
995 security: the challenge of feeding 9 billion people. *Science* **327**, 812–818.

996 **Graumann, K., Runions, J. and Evans, D. E.** (2010). Characterization of SUN-domain
997 proteins at the higher plant nuclear envelope. *Plant J.* **61**, 134–144.

998 **Graumann, K., Vanrobays, E., Tutois, S., Probst, A. V., Evans, D. E. and Tatout, C.**
999 (2014). Characterization of two distinct subfamilies of SUN-domain proteins in
1000 Arabidopsis and their interactions with the novel KASH-domain protein AtTIK. *J.*
1001 *Exp. Bot.* **65**, 6499–6512.

1002 **Griffis, A. H. N., Groves, N. R., Zhou, X. and Meier, I.** (2014). Nuclei in motion:
1003 movement and positioning of plant nuclei in development, signaling, symbiosis, and
1004 disease. *Front. Plant Sci.* **5**, 129.

1005 **Groves, N. R., Biel, A. M., Newman-Griffis, A. H. and Meier, I.** (2018). Dynamic
1006 Changes in Plant Nuclear Organization in Response to Environmental and
1007 Developmental Signals. *Plant Physiol.* **176**, 230–241.

1008 **Gumber, H. K., McKenna, J. F., Estrada, A. L., Tolmie, A. F., Graumann, K. and**
1009 **Bass, H. W.** (2019). Identification and characterization of genes encoding the
1010 nuclear envelope LINC complex in the monocot species Zea mays. *J. Cell Sci.* **132**,
1011 1–16.

1012 **Gundersen, G. G. and Worman, H. J.** (2013). Nuclear positioning. *Cell* **152**, 1376–
1013 1389.

1014 **Hagan, I. and Yanagida, M.** (1995). The product of the spindle formation gene sad1+
1015 associates with the fission yeast spindle pole body and is essential for viability. *J.*
1016 *Cell Biol.* **129**, 1033–1047.

1017 **Hatzfeld, M.** (1998). The Armadillo Family of Structural Proteins. In *International*
1018 *Review of Cytology* (ed. Jeon, K. W.), pp. 179–224. Academic Press.

1019 **Hawkins, T. J., Deeks, M. J., Wang, P. and Hussey, P. J.** (2014). The evolution of the
1020 actin binding NET superfamily. *Front. Plant Sci.* **5**, 254.

1021 **Hetzer, M. W.** (2010). The nuclear envelope. *Cold Spring Harb. Perspect. Biol.* **2**,
1022 a000539.

1023 **Hieda, M.** (2017). Implications for Diverse Functions of the LINC Complexes Based on
1024 the Structure. *Cells* **6**,.

1025 **Higgins, D. M., Nannas, N. J. and Dawe, R. K.** (2016). The Maize Divergent spindle-1
1026 (dv1) Gene Encodes a Kinesin-14A Motor Protein Required for Meiotic Spindle
1027 Pole Organization. *Front. Plant Sci.* **7**, 1277.

1028 **Howe, E. S., Murphy, S. P. and Bass, H. W.** (2013). Three-Dimensional Acrylamide
1029 Fluorescence In Situ Hybridization for Plant Cells. In *Plant Meiosis: Methods and*
1030 *Protocols* (ed. Pawlowski, W. P.), Grelon, M.), and Armstrong, S.), pp. 53–66.
1031 Totowa, NJ: Humana Press.

1032 **Huelsmann, S. and Brown, N. H.** (2014). Nuclear positioning by actin cables and
1033 perinuclear actin: Special and general? *Nucleus* **5**, 219–223.

1034 **Janin, A., Bauer, D., Ratti, F., Millat, G. and Méjat, A.** (2017). Nuclear envelopathies:
1035 a complex LINC between nuclear envelope and pathology. *Orphanet J. Rare Dis.*
1036 **12**, 147.

1037 **Karimi, M., Inzé, D. and Depicker, A.** (2002). GATEWAY^{TM} vectors for Agrobacterium-
1038 mediated plant transformation. *Trends Plant Sci.* **7**, 193–195.

1039 **Kim, D. I., Birendra, K. C. and Roux, K. J.** (2015). Making the LINC: SUN and KASH
1040 protein interactions. *Biol. Chem.* **396**, 295–310.

1041 **Labonne, J. D. J., Dorweiler, J. E. and McGinnis, K. M.** (2013). Changes in
1042 nucleosome position at transcriptional start sites of specific genes in Zea mays
1043 mediator of paramutation1 mutants. *Epigenetics* **8**, 398–408.

1044 **Lin, F., Jiang, L., Liu, Y., Lv, Y., Dai, H. and Zhao, H.** (2014). Genome-wide
1045 identification of housekeeping genes in maize. *Plant Mol. Biol.* **86**, 543–554.

1046 **Link, J., Leubner, M., Schmitt, J., Göb, E., Benavente, R., Jeang, K.-T., Xu, R. and**
1047 **Alsheimer, M.** (2014). Analysis of meiosis in SUN1 deficient mice reveals a distinct
1048 role of SUN2 in mammalian meiotic LINC complex formation and function. *PLoS*
1049 *Genet.* **10**, e1004099.

1050 **Livak, K. J. and Schmittgen, T. D.** (2001). Analysis of relative gene expression data
1051 using real-time quantitative PCR and the 2- ΔΔCT method. *Methods* **25**, 402–408.

1052 **Luxton, G. W. G. and Starr, D. A.** (2014). KASHing up with the nucleus: novel
1053 functional roles of KASH proteins at the cytoplasmic surface of the nucleus. *Curr.*
1054 *Opin. Cell Biol.* **28**, 69–75.

1055 **Malone, C. J., Fixsen, W. D., Horvitz, H. R. and Han, M.** (1999). UNC-84 localizes to
1056 the nuclear envelope and is required for nuclear migration and anchoring during C.
1057 elegans development. *Development* **126**, 3171–3181.

1058 **Martinière, A., Lavagi, I., Nageswaran, G., Rolfe, D. J., Maneta-Peyret, L., Luu, D.-**
1059 **T., Botchway, S. W., Webb, S. E. D., Mongrand, S., Maurel, C., et al.** (2012). Cell
1060 wall constrains lateral diffusion of plant plasma-membrane proteins. *Proc. Natl.*
1061 *Acad. Sci. U. S. A.* **109**, 12805–12810.

1062 **McCarty, D. R. and Meeley, R. B.** (2009). Transposon Resources for Forward and
1063 Reverse Genetics in Maize. In *Handbook of Maize: Genetics and Genomics* (ed.
1064 Bennetzen, J. L.) and Hake, S.), pp. 561–584. New York, NY: Springer New York.

1065 **McCarty, D. R., Suzuki, M., Hunter, C., Collins, J., Avigne, W. T. and Koch, K. E.**
1066 (2013). Genetic and Molecular Analyses of UniformMu Transposon Insertion Lines.
1067 In *Plant Transposable Elements: Methods and Protocols* (ed. Peterson, T.), pp.

1068 157–166. Totowa, NJ: Humana Press.

1069 **Meier, I.** (2016). LINCing the eukaryotic tree of life - towards a broad evolutionary
1070 comparison of nucleocytoplasmic bridging complexes. *J. Cell Sci.* **129**, 3523–3531.

1071 **Meier, I., Zhou, X., Brkljacić, J., Rose, A., Zhao, Q. and Xu, X. M.** (2010). Targeting
1072 proteins to the plant nuclear envelope. *Biochem. Soc. Trans.* **38**, 733–740.

1073 **Meier, I., Richards, E. J. and Evans, D. E.** (2017). Cell Biology of the Plant Nucleus.
1074 *Annu. Rev. Plant Biol.* **68**, 139–172.

1075 **Moriguchi, K., Suzuki, T., Ito, Y., Yamazaki, Y., Niwa, Y. and Kurata, N.** (2005).
1076 Functional isolation of novel nuclear proteins showing a variety of subnuclear
1077 localizations. *Plant Cell* **17**, 389–403.

1078 **Müller, S., Wright, A. J. and Smith, L. G.** (2009). Division plane control in plants: new
1079 players in the band. *Trends Cell Biol.* **19**, 180–188.

1080 **Murphy, S. P., Gumber, H. K., Mao, Y. and Bass, H. W.** (2014). A dynamic meiotic
1081 SUN belt includes the zygotene-stage telomere bouquet and is disrupted in
1082 chromosome segregation mutants of maize (Zea mays L.). *Front. Plant Sci.* **5**, 314.

1083 **Newman-Griffis, A. H., Del Cerro, P., Charpentier, M. and Meier, I.** (2019). Medicago
1084 LINC Complexes Function in Nuclear Morphology, Nuclear Movement, and Root
1085 Nodule Symbiosis. *Plant Physiol.* **179**, 491–506.

1086 **Oda, Y. and Fukuda, H.** (2011). Dynamics of Arabidopsis SUN proteins during mitosis
1087 and their involvement in nuclear shaping. *Plant J.* **66**, 629–641.

1088 **Peterson, R., Slovin, J. P. and Chen, C.** (2010). A simplified method for differential
1089 staining of aborted and non-aborted pollen grains. *1* **1**, e13–e13.

1090 **Poulet, A., Probst, A. V., Graumann, K., Tatout, C. and Evans, D.** (2017a). Exploring
1091 the evolution of the proteins of the plant nuclear envelope. *Nucleus* **8**, 46–59.

1092 **Poulet, A., Duc, C., Voisin, M., Desset, S., Tutois, S., Vanrobays, E., Benoit, M.,**
1093 **Evans, D. E., Probst, A. V. and Tatout, C.** (2017b). The LINC complex contributes
1094 to heterochromatin organisation and transcriptional gene silencing in plants. *J. Cell*
1095 *Sci.* **130**, 590–601.

1096 **Sakamoto, Y. and Takagi, S.** (2013). LITTLE NUCLEI 1 and 4 regulate nuclear
1097 morphology in Arabidopsis thaliana. *Plant Cell Physiol.* **54**, 622–633.

1098 **Settles, A. M., Holding, D. R., Tan, B. C., Latshaw, S. P., Liu, J., Suzuki, M., Li, L.,**
1099 **O'Brien, B. A., Fajardo, D. S., Wroclawska, E., et al.** (2007). Sequence-indexed
1100 mutations in maize using the UniformMu transposon-tagging population. *BMC*
1101 *Genomics* **8**, 116.

1102 **Shamina, N. V.** (2003). [Dynamics of cytoskeleton microtubules in higher plant meiosis.
1103 I. The perinuclear band of microtubules and the meiotic spindle formation].
1104 *Tsitologiia* **45**, 650–654.

1105 **Sheehan, M. J. and Pawlowski, W. P.** (2009). Live imaging of rapid chromosome
1106 movements in meiotic prophase I in maize. *Proc. Natl. Acad. Sci. U. S. A.* **106**,
1107 20989–20994.

1108 **Smith, L. G.** (2001). Plant cell division: building walls in the right places. *Nat. Rev. Mol.*
1109 *Cell Biol.* **2**, 33–39.

1110 **Sosa, B. A., Rothballer, A., Kutay, U. and Schwartz, T. U.** (2012). LINC complexes
1111 form by binding of three KASH peptides to domain interfaces of trimeric SUN
1112 proteins. *Cell* **149**, 1035–1047.

1113 **Sparkes, I. A., Runions, J., Kearns, A. and Hawes, C.** (2006). Rapid, transient
1114 expression of fluorescent fusion proteins in tobacco plants and generation of stably
1115 transformed plants. *Nat. Protoc.* **1**, 2019–2025.

1116 **Springer, N. M., Anderson, S. N., Andorf, C. M., Ahern, K. R., Bai, F., Barad, O.,**
1117 **Barbazuk, W. B., Bass, H. W., Baruch, K., Ben-Zvi, G., et al.** (2018). The maize
1118 W22 genome provides a foundation for functional genomics and transposon
1119 biology. *Nat. Genet.* **50**, 1282–1288.

1120 **Starr, D. A. and Fridolfsson, H. N.** (2010). Interactions between nuclei and the
1121 cytoskeleton are mediated by SUN-KASH nuclear-envelope bridges. *Annu. Rev.*
1122 *Cell Dev. Biol.* **26**, 421–444.

1123 **Starr, D. A. and Han, M.** (2002). Role of ANC-1 in tethering nuclei to the actin
1124 cytoskeleton. *Science* **298**, 406–409.

1125 **Stelpflug, S. C., Sekhon, R. S., Vaillancourt, B., Hirsch, C. N., Buell, C. R., de Leon,**
1126 **N. and Kaeppler, S. M.** (2016). An Expanded Maize Gene Expression Atlas based
1127 on RNA Sequencing and its Use to Explore Root Development. *Plant Genome* **9**,.

1128 **Tamura, K., Iwabuchi, K., Fukao, Y., Kondo, M., Okamoto, K., Ueda, H., Nishimura,**
1129 **M. and Hara-Nishimura, I.** (2013). Myosin XI-i links the nuclear membrane to the
1130 cytoskeleton to control nuclear movement and shape in Arabidopsis. *Curr. Biol.* **23**,
1131 1776–1781.

1132 **Thomas, J. B. and Kaltsikes, P. J.** (1977). THE EFFECT OF COLCHICINE ON
1133 CHROMOSOME PAIRING. *Can. J. Genet. Cytol.* **19**, 231–249.

1134 **Uzer, G., Rubin, C. T. and Rubin, J.** (2016). Cell Mechanosensitivity is Enabled by the
1135 LINC Nuclear Complex. *Curr Mol Biol Rep* **2**, 36–47.

1136 **Van de Vosse, D. W., Wan, Y., Wozniak, R. W. and Aitchison, J. D.** (2011). Role of
1137 the nuclear envelope in genome organization and gene expression. *Wiley*

1138 *Interdiscip. Rev. Syst. Biol. Med.* **3**, 147–166.

1139 **Varas, J., Graumann, K., Osman, K., Pradillo, M., Evans, D. E., Santos, J. L. and**
1140 **Armstrong, S. J.** (2015). Absence of SUN1 and SUN2 proteins in Arabidopsis
1141 thaliana leads to a delay in meiotic progression and defects in synapsis and
1142 recombination. *Plant J.* **81**, 329–346.

1143 **Wang, S., Stoops, E., Cp, U., Markus, B., Reuveny, A., Ordan, E. and Volk, T.**
1144 (2018). Mechanotransduction via the LINC complex regulates DNA replication in
1145 myonuclei. *J. Cell Biol.* **217**, 2005–2018.

1146 **Xu, X. M., Meulia, T. and Meier, I.** (2007). Anchorage of plant RanGAP to the nuclear
1147 envelope involves novel nuclear-pore-associated proteins. *Curr. Biol.* **17**, 1157–
1148 1163.

1149 **Zhou, X. and Meier, I.** (2013). How plants LINC the SUN to KASH. *Nucleus* **4**, 206–
1150 215.

1151 **Zhou, X., Graumann, K., Evans, D. E. and Meier, I.** (2012). Novel plant SUN–KASH
1152 bridges are involved in RanGAP anchoring and nuclear shape determination. *J.*
1153 *Cell Biol.* **196**, 203–211.

1154 **Zhou, X., Graumann, K., Wirthmueller, L., Jones, J. D. G. and Meier, I.** (2014).
1155 Identification of unique SUN-interacting nuclear envelope proteins with diverse
1156 functions in plants. *J. Cell Biol.* **205**, 677–692.

1157 **Zhou, X., Groves, N. R. and Meier, I.** (2015a). Plant nuclear shape is independently
1158 determined by the SUN-WIP-WIT2-myosin XI-i complex and CRWN1. *Nucleus* **6**,
1159 144–153.

1160 **Zhou, X., Groves, N. R. and Meier, I.** (2015b). SUN anchors pollen WIP-WIT
1161 complexes at the vegetative nuclear envelope and is necessary for pollen tube
1162 targeting and fertility. *J. Exp. Bot.* **66**, 7299–7307.

1163

A

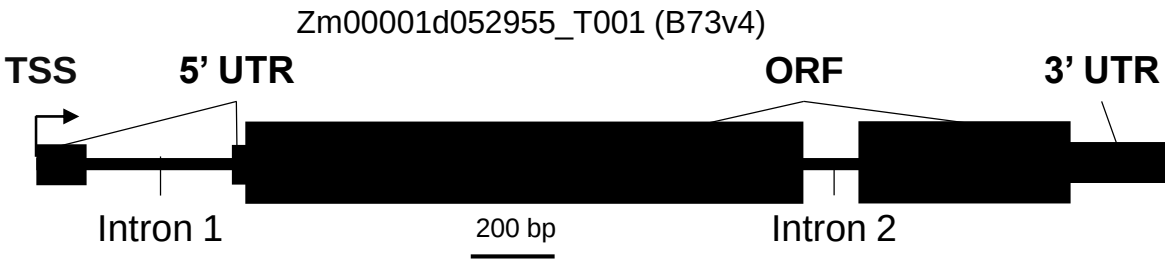

B

```
  1 MGRSLSPLLR QELDNLDKDA DSRRAAMKAL KSYARHLDSK SIPHFLAEVS DTTAAGAGAG
 61 SGMPTGGEFT ISLYEVLARV HGRNIVPQIG NIMATIMCTL SSSGGSFPLH QACSKVVPAI
121 ARHGIDPSAP DGEKAGIIAS LCRPLCSALM GGSQDGGAAS GAALCLKALV ESSNWRFASG
181 ELVNEVCLKV AGAMHDSATR SNAHMGLAMA LVKHNGLIAE AYARSIVRSG LQILDGDTAD
241 SSSQKRLSAI QMINFFMKFV DPRCLSSELG RVIDVMERCQ NDRMPFVRGA AFEASQSARN
301 IAAQKGSRHE VGTSPMVGSN FHKRREKSPC RSLWGAKRSP AASTMAAASP VQFRSPESQV
361 VDSSIMNGST LHDSPVSVGQ SSCNFDQSRR TNRRLWSNDA VDVSLKDGLF IQLCSNSNSY
421 EDDLGEVCDS EVTDANFECT NTFAGFVSPS HNGSISRDKT PSPRASDRPI NIDDVKIYST
481 PRKLLRLLQS SYDSDSASNI GQSTAKLRGL SSPDQEHKGL VISSEQMQSL HSDNKGDEMK
541 DENETIYMQN SKGRTQTLSN ADASVLSTTE AENTSIKTSP EIELNGDDVC ITSSIGKTRK
601 YRAKFTLFLS VIVIFLAIIT MLIRIENDDD SAYLVPT*
```

α-helix Transmembrane domain KASH domain

C

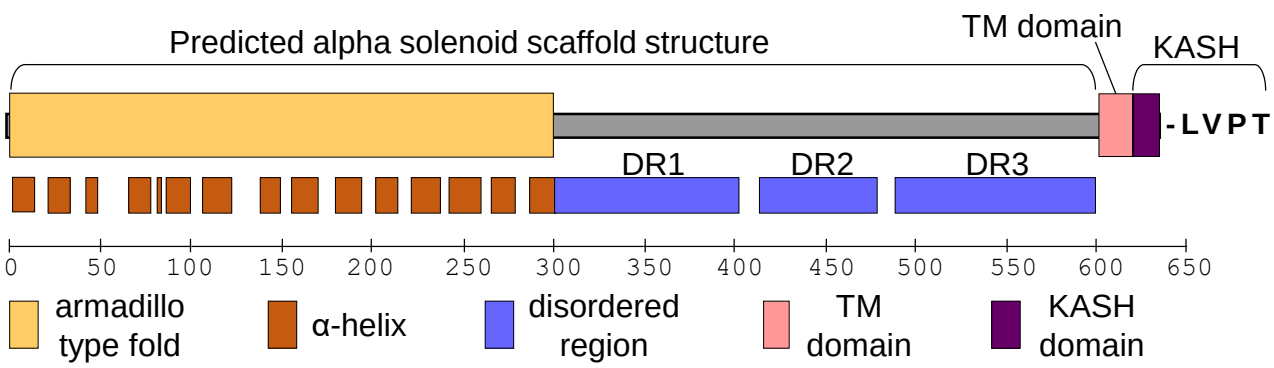

D

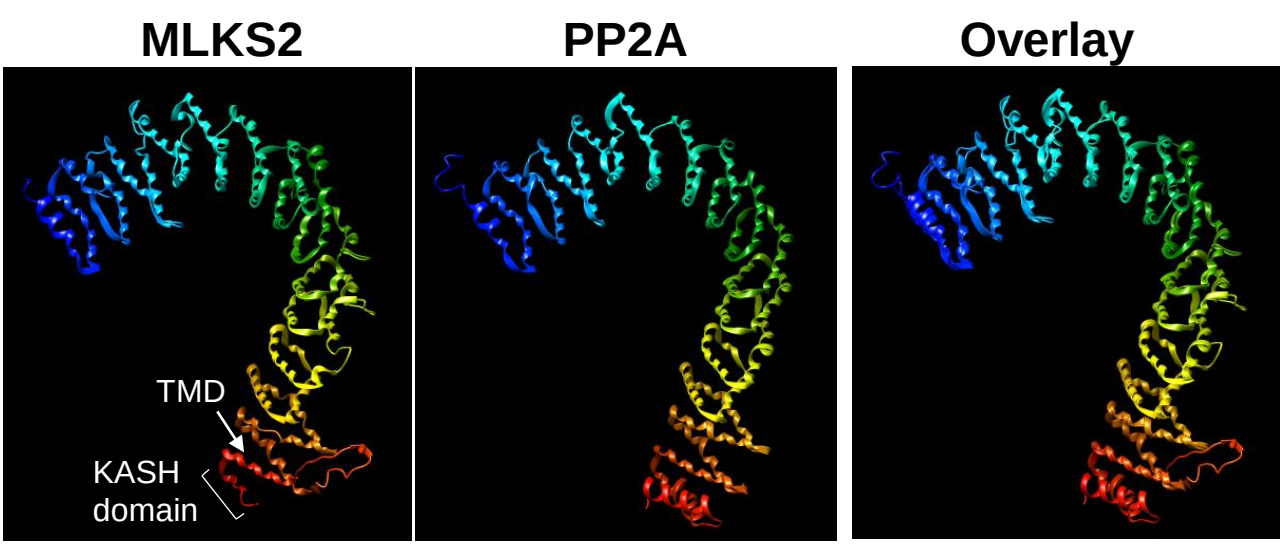

Figure 1

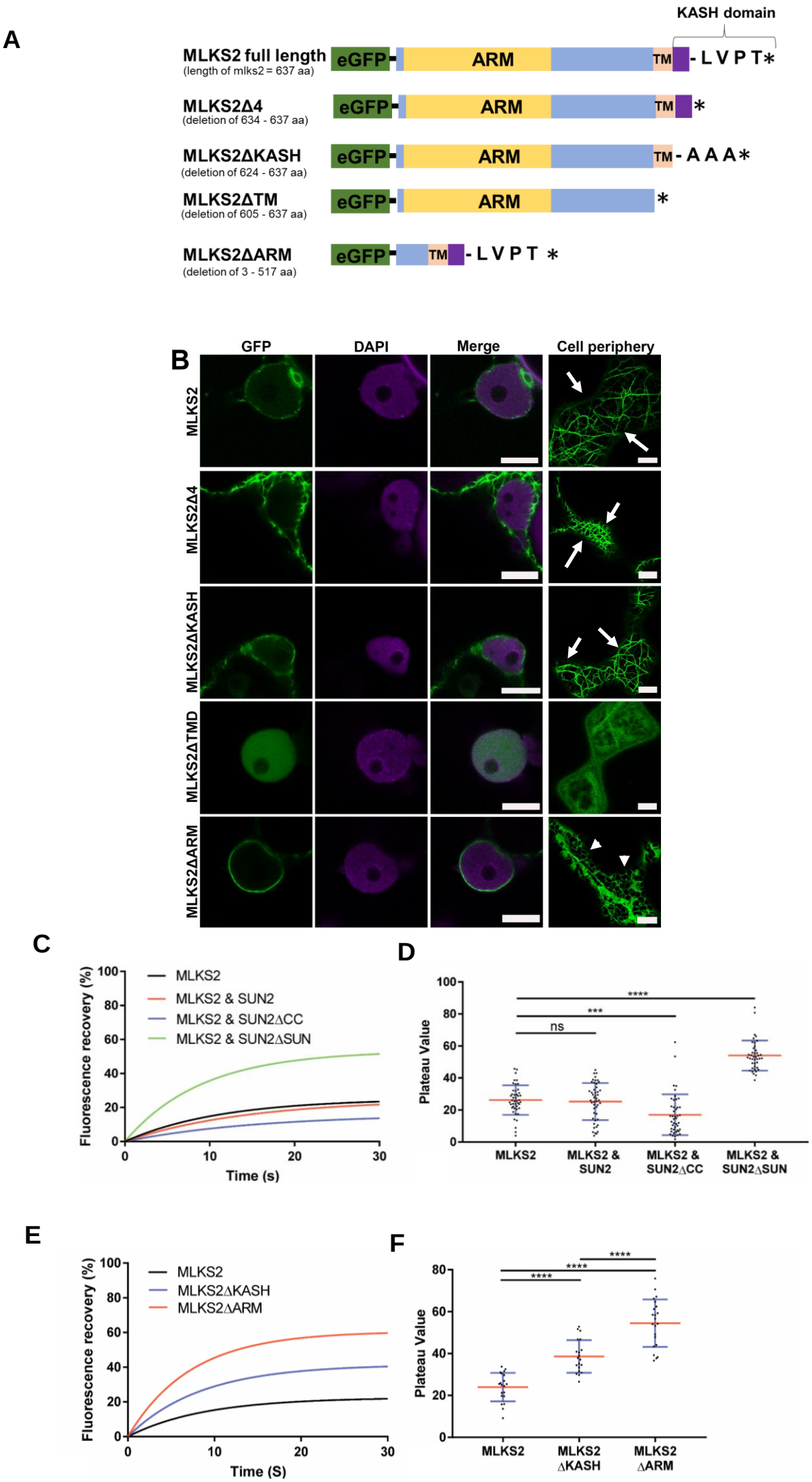
A
KASH domain
MLKS2 full length
(length of mlks2 = 637 aa)
eGFP
ARM
TM
- L V P T*
MLKS2Δ4
(deletion of 634 - 637 aa)
MLKS2ΔKASH
(deletion of 624 - 637 aa)
- A A A*
MLKS2ΔTM
(deletion of 605 - 637 aa)
MLKS2ΔARM
(deletion of 3 - 517 aa)
B
GFP
DAPI
Merge
Cell periphery
MLKS2
MLKS2Δ4
MLKS2ΔKASH
MLKS2ΔTMD
MLKS2ΔARM
C
Fluorescence recovery (%)
Time (s)
MLKS2
MLKS2 & SUN2
MLKS2 & SUN2ΔCC
MLKS2 & SUN2ΔSUN
D
Plateau Value
ns
***
****
MLKS2
MLKS2 & SUN2
MLKS2 & SUN2ΔCC
MLKS2 & SUN2ΔSUN
E
Fluorescence recovery (%)
Time (S)
MLKS2
MLKS2ΔKASH
MLKS2ΔARM
F
Plateau Value
****
MLKS2
MLKS2 ΔKASH
MLKS2 ΔARM

Figure 2

A

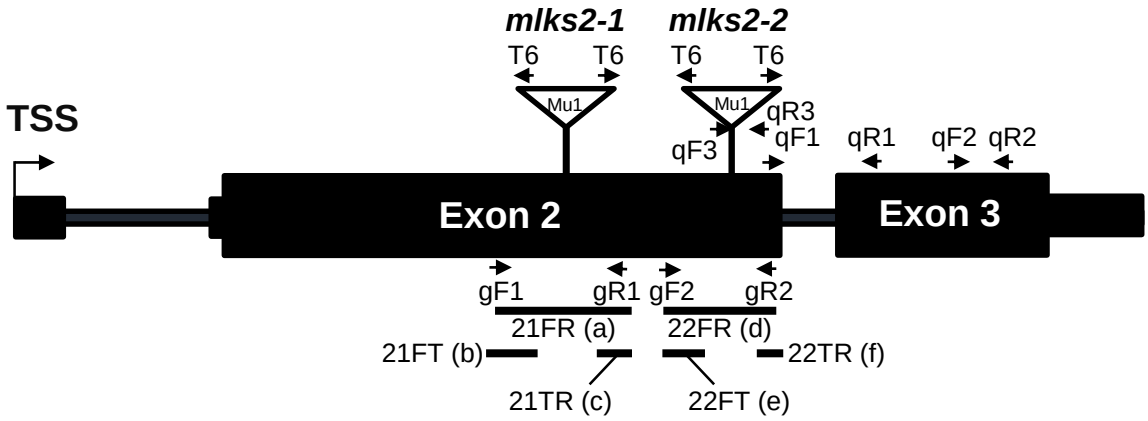

B

```
MLKS2 published      GCCAGAATGACCGCATGCCTTTCGTCCGAGGTGCTGCGTTTGAGGCATC
MLKS2 PCR 21FR(a)    GCCAGAATGACCGCATGCCTTTCGTCCGAGGTGCTGCGTTTGAGGCATC
mlks2-1 PCR 21FT(b)  GCCAGAATGACCGCATGCCTTTCGTCCGAgagataa...
mlks2-1 PCR 21TR(c)            ...ttatctcTTCGTCCGAGGTGCTGCGTTTGAGGCATC

MLKS2 published      AGCAATTCCTATGAAGATGACTTGGGCGAGGTCTGTGACAGTGAAGTGA
MLKS2 PCR 22FR(d)    AGCAATTCCTATGAAGATGACTTGGGCGAGGTCTGTGACAGTGAAGTGA
mlks2-2 PCR 22FT(e)  AGCAATTCCTATGAAGATGACTTGGGCGAgagataatt...
mlks2-2 PCR 22TR(f)            ...ttatctcCTTGGGCGAGGTCTGTGACAGTGAAGTGA
```

C

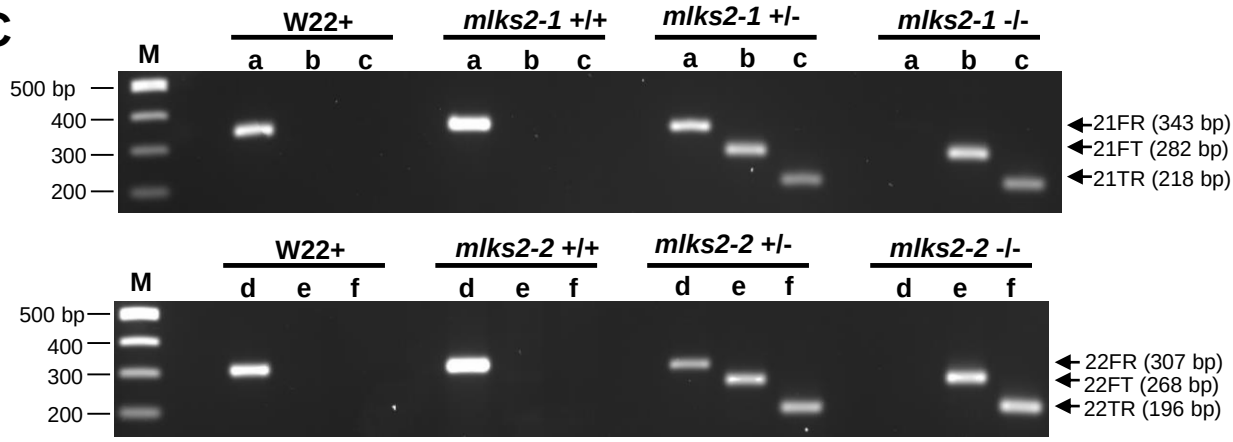

D

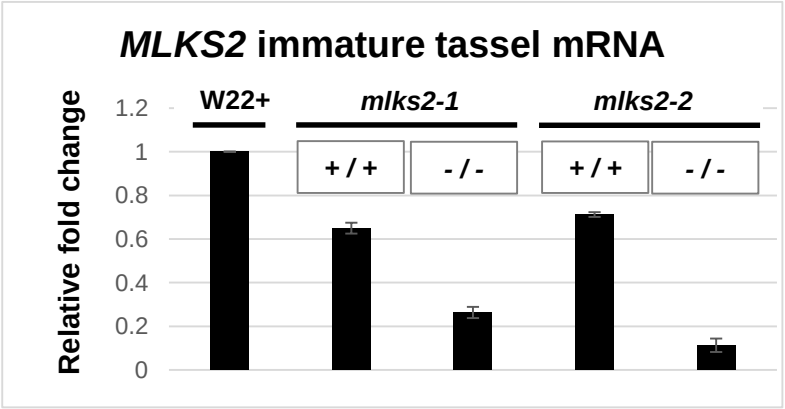

Figure 3

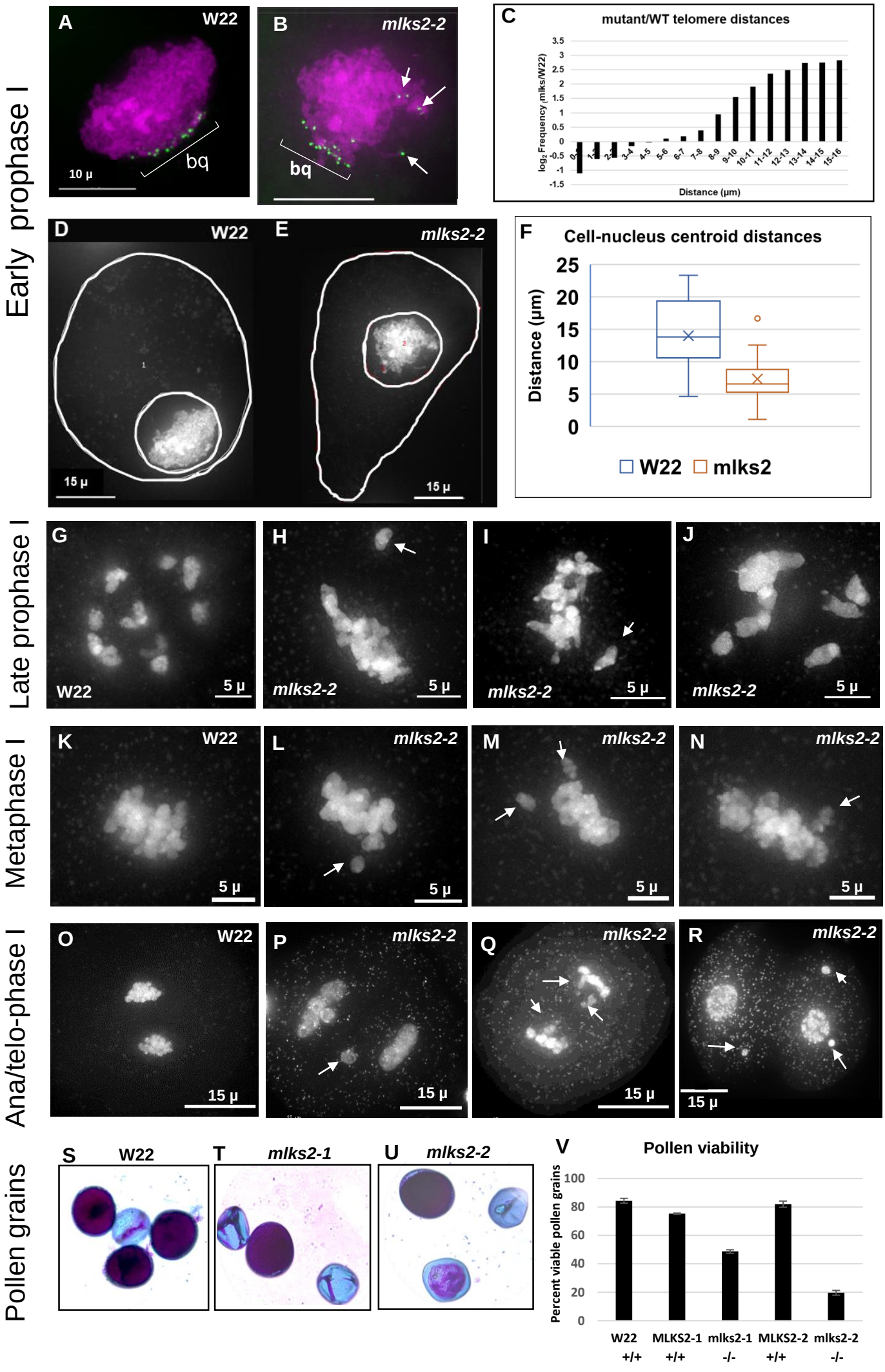
Early prophase I
A
W22
10 µ
bq
B
mlks2-2
bq
C
mutant/WT telomere distances
log2 Frequency (mlks/W22)
Distance (µm)
D
W22
15 µ
E
mlks2-2
15 µ
F
Cell-nucleus centroid distances
Distance (µm)
W22
mlks2
Late prophase I
G
W22
5 µ
H
mlks2-2
5 µ
I
mlks2-2
5 µ
J
mlks2-2
5 µ
Metaphase I
K
W22
5 µ
L
mlks2-2
5 µ
M
mlks2-2
5 µ
N
mlks2-2
5 µ
Ana/telo-phase I
O
W22
15 µ
P
mlks2-2
15 µ
Q
mlks2-2
15 µ
R
mlks2-2
15 µ
Pollen grains
S
W22
T
mlks2-1
U
mlks2-2
V
Pollen viability
Percent viable pollen grains
W22 +/+
MLKS2-1 +/+
mlks2-1 -/-
MLKS2-2 +/+
mlks2-2 -/-

Figure 4

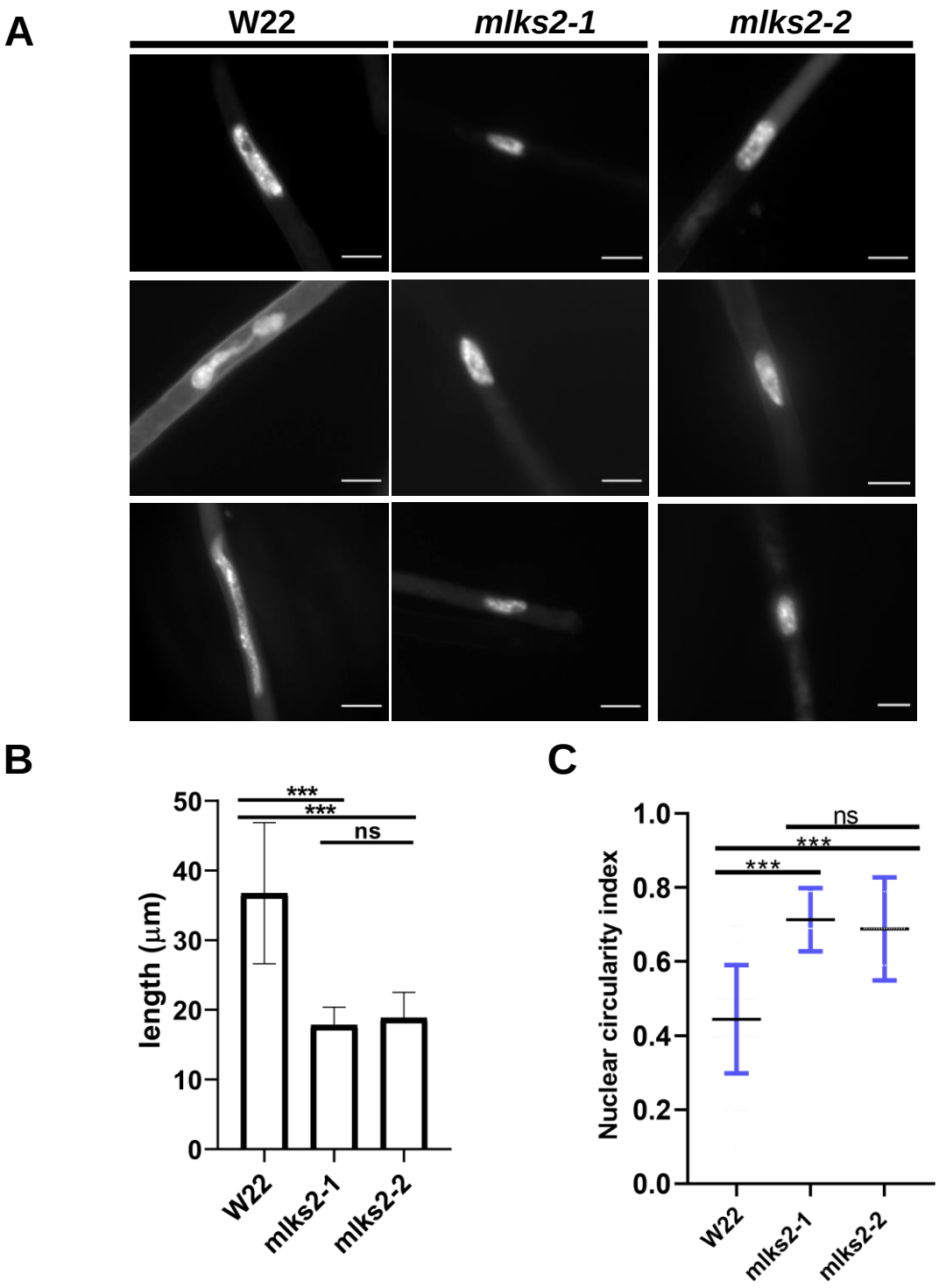
A
W22
mlks2-1
mlks2-2
B
length (μm)
50
40
30
20
10
0
***
***
ns
W22
mlks2-1
mlks2-2
C
Nuclear circularity index
1.0
0.8
0.6
0.4
0.2
0.0
ns
***
***
W22
mlks2-1
mlks2-2

Figure 5

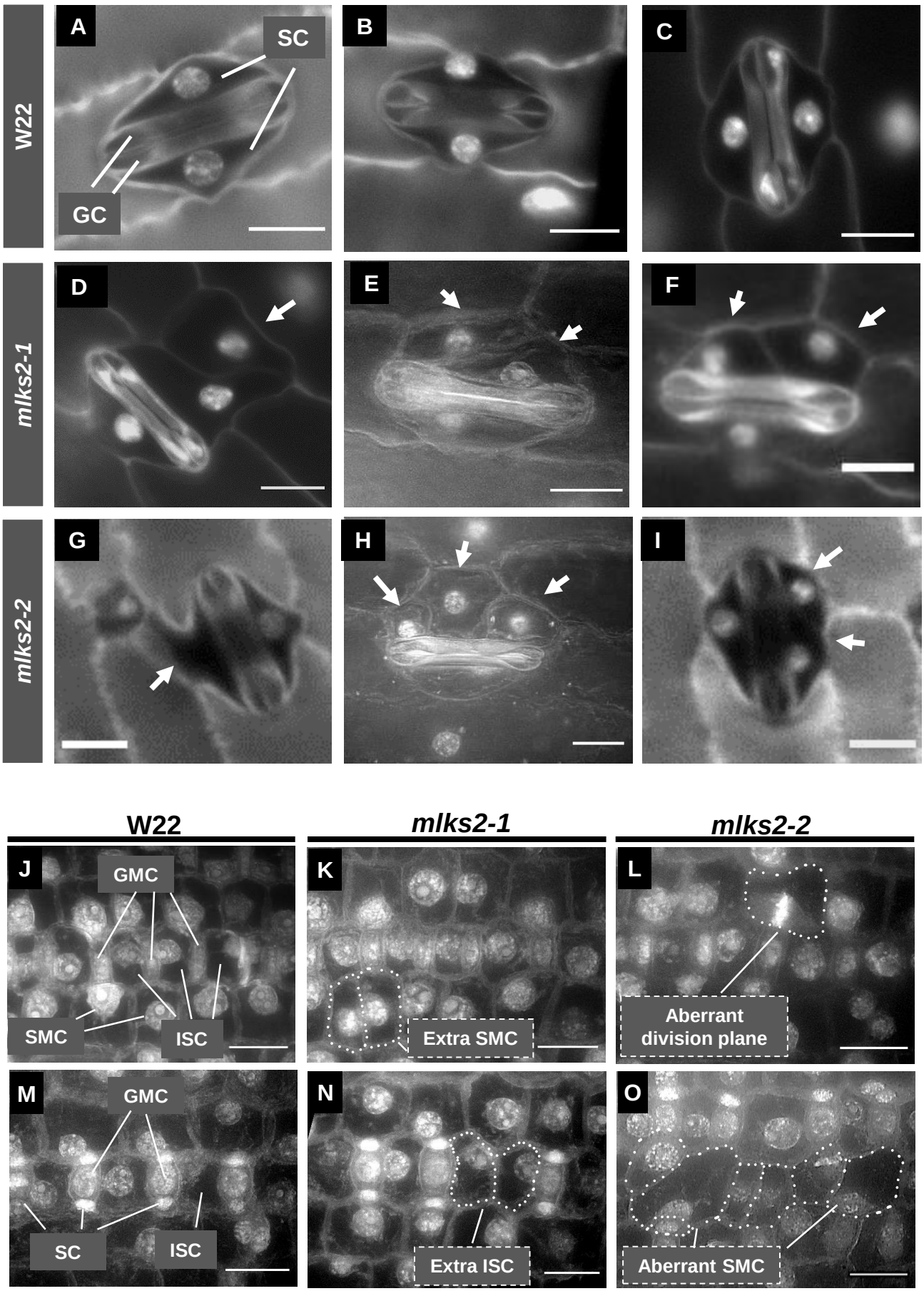
W22
mlks2-1
mlks2-2
A
SC
GC
B
C
D
E
F
G
H
I
W22
mlks2-1
mlks2-2
J
GMC
SMC
ISC
K
Extra SMC
L
Aberrant
division plane
M
GMC
SC
ISC
N
Extra ISC
O
Aberrant SMC

Figure 6

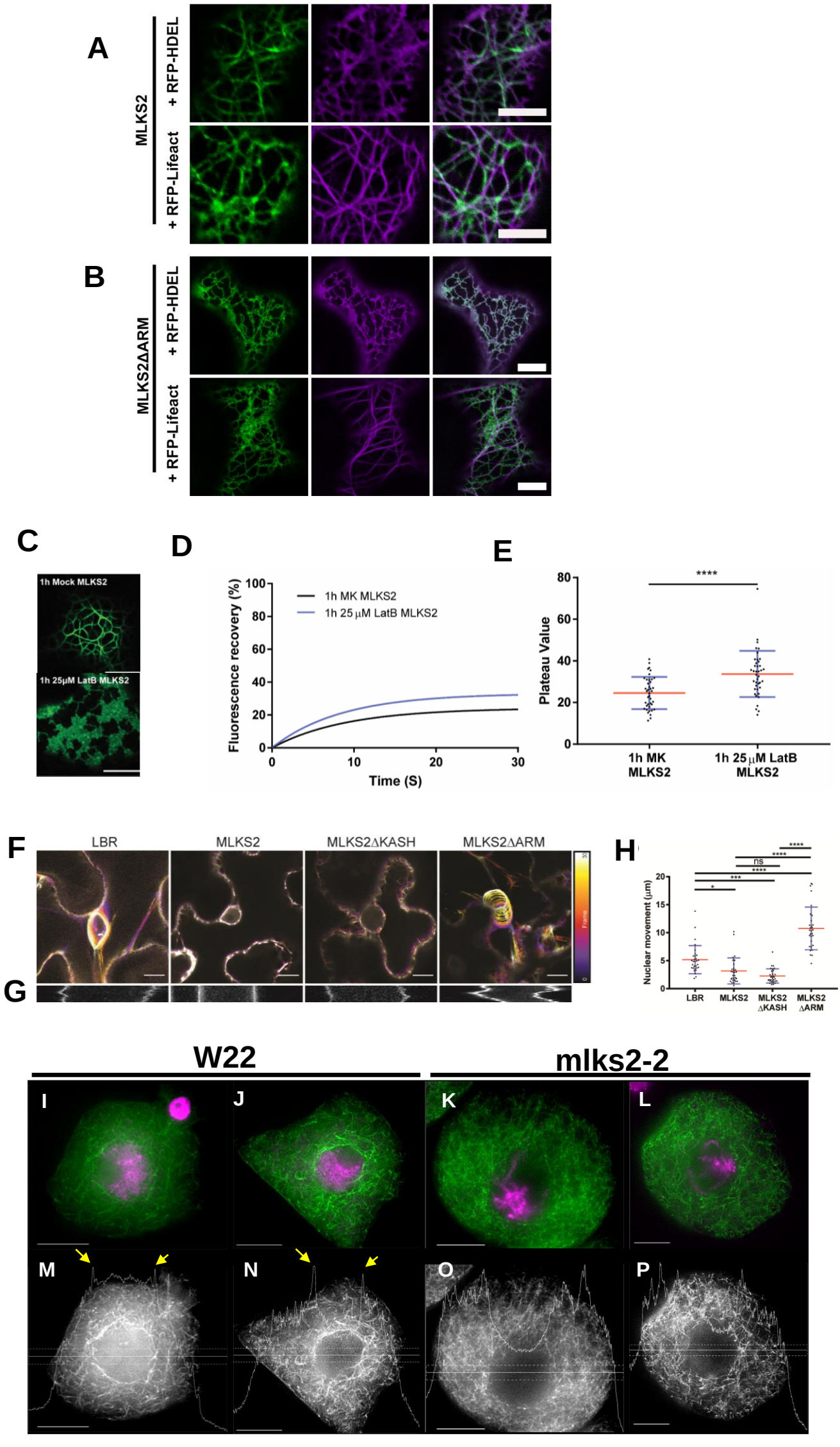
A
MLKS2
+ RFP-HDEL
+ RFP-Lifeact
B
MLKS2ΔARM
+ RFP-HDEL
+ RFP-Lifeact
C
1h Mock MLKS2
1h 25μM LatB MLKS2
D
Fluorescence recovery (%)
1h MK MLKS2
1h 25 μM LatB MLKS2
Time (S)
E
Plateau Value
****
1h MK MLKS2
1h 25 μM LatB MLKS2
F
LBR
MLKS2
MLKS2ΔKASH
MLKS2ΔARM
G
H
Nuclear movement (μm)
ns
LBR
MLKS2
MLKS2 ΔKASH
MLKS2 ΔARM
W22
mlks2-2
I
J
K
L
M
N
O
P

Figure 7

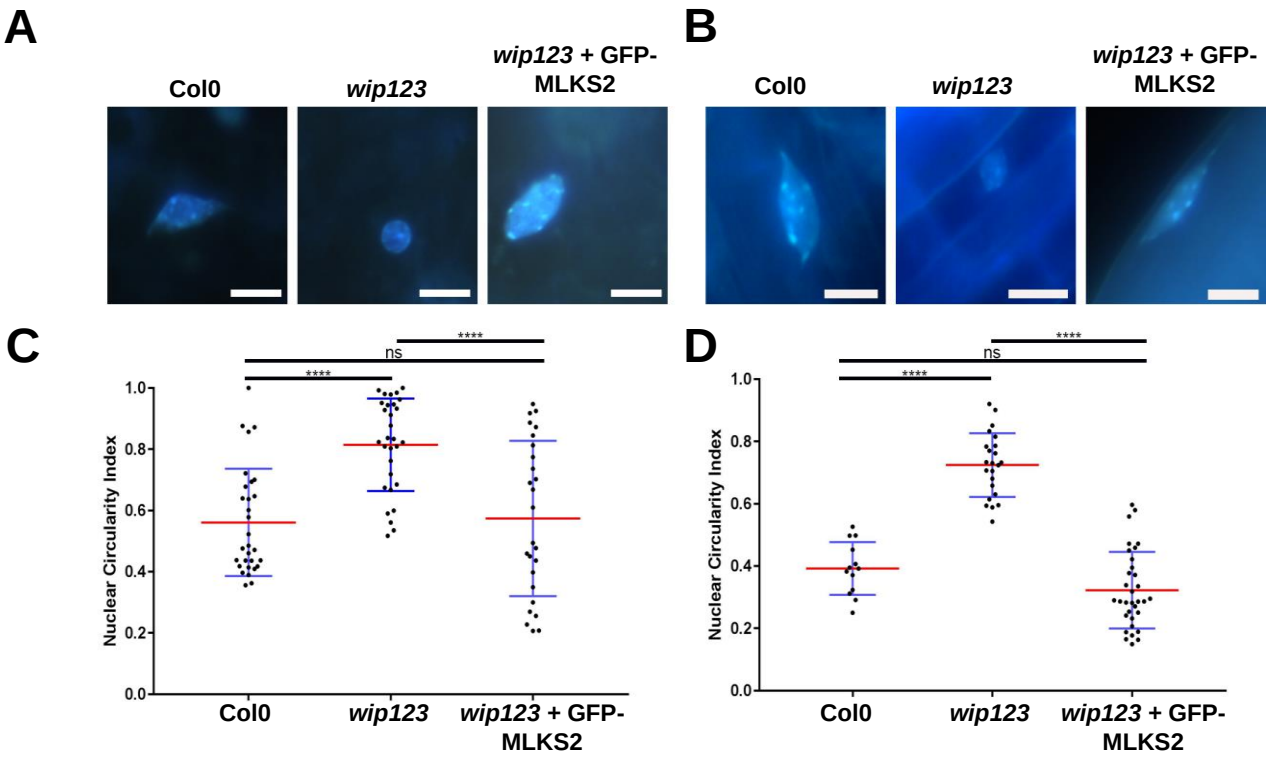
A
Col0
wip123
wip123 + GFP-MLKS2
B
Col0
wip123
wip123 + GFP-MLKS2
C
Nuclear Circularity Index
1.0
0.8
0.6
0.4
0.2
0.0
****
ns
****
Col0
wip123
wip123 + GFP-MLKS2
D
Nuclear Circularity Index
1.0
0.8
0.6
0.4
0.2
0.0
****
ns
****
Col0
wip123
wip123 + GFP-MLKS2

Figure 8

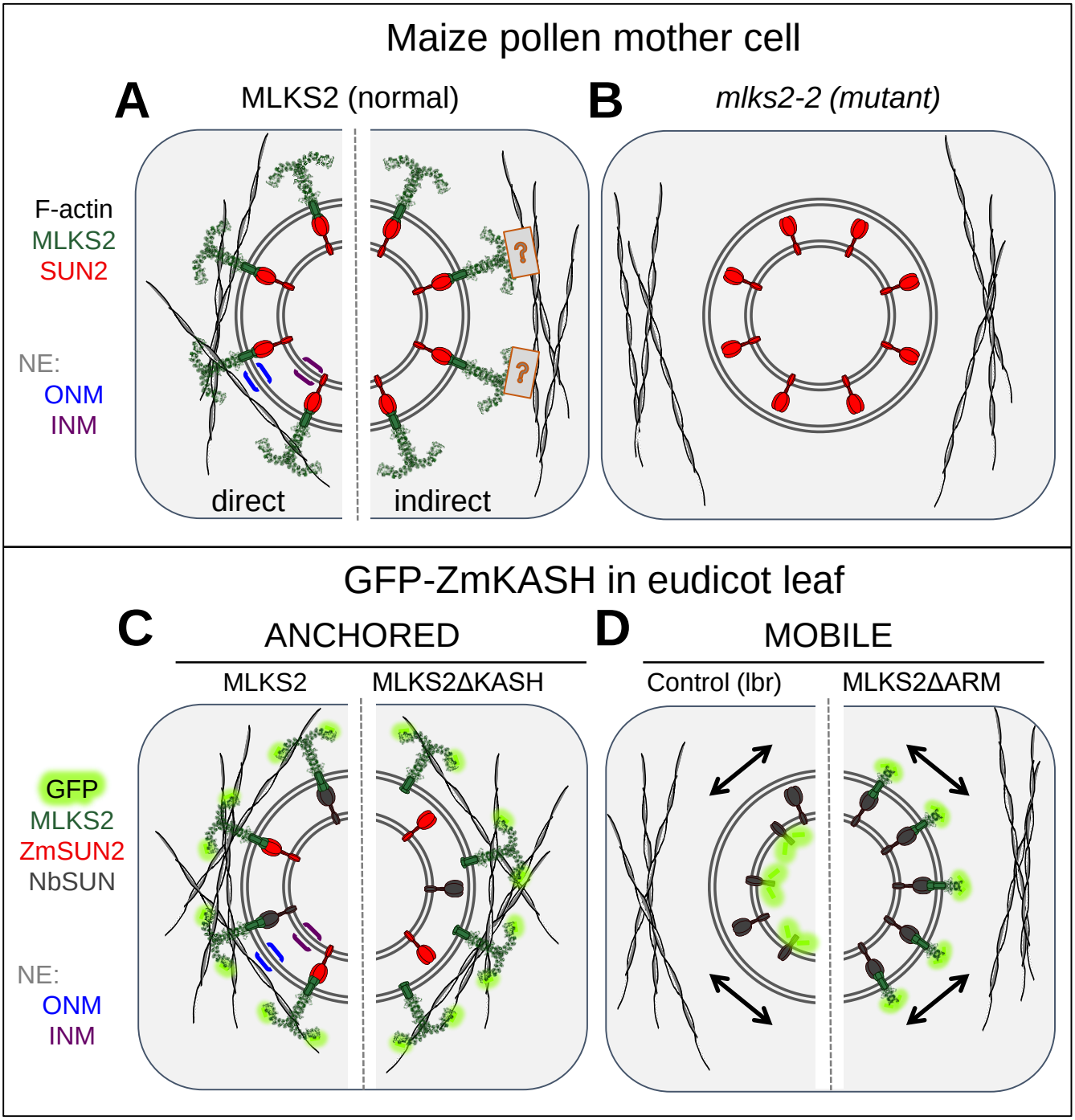
Maize pollen mother cell
A
MLKS2 (normal)
B
mlks2-2 (mutant)
F-actin
MLKS2
SUN2
NE:
ONM
INM
direct
indirect
GFP-ZmKASH in eudicot leaf
C
ANCHORED
D
MOBILE
MLKS2
MLKS2ΔKASH
Control (lbr)
MLKS2ΔARM
GFP
MLKS2
ZmSUN2
NbSUN
NE:
ONM
INM

Figure 9

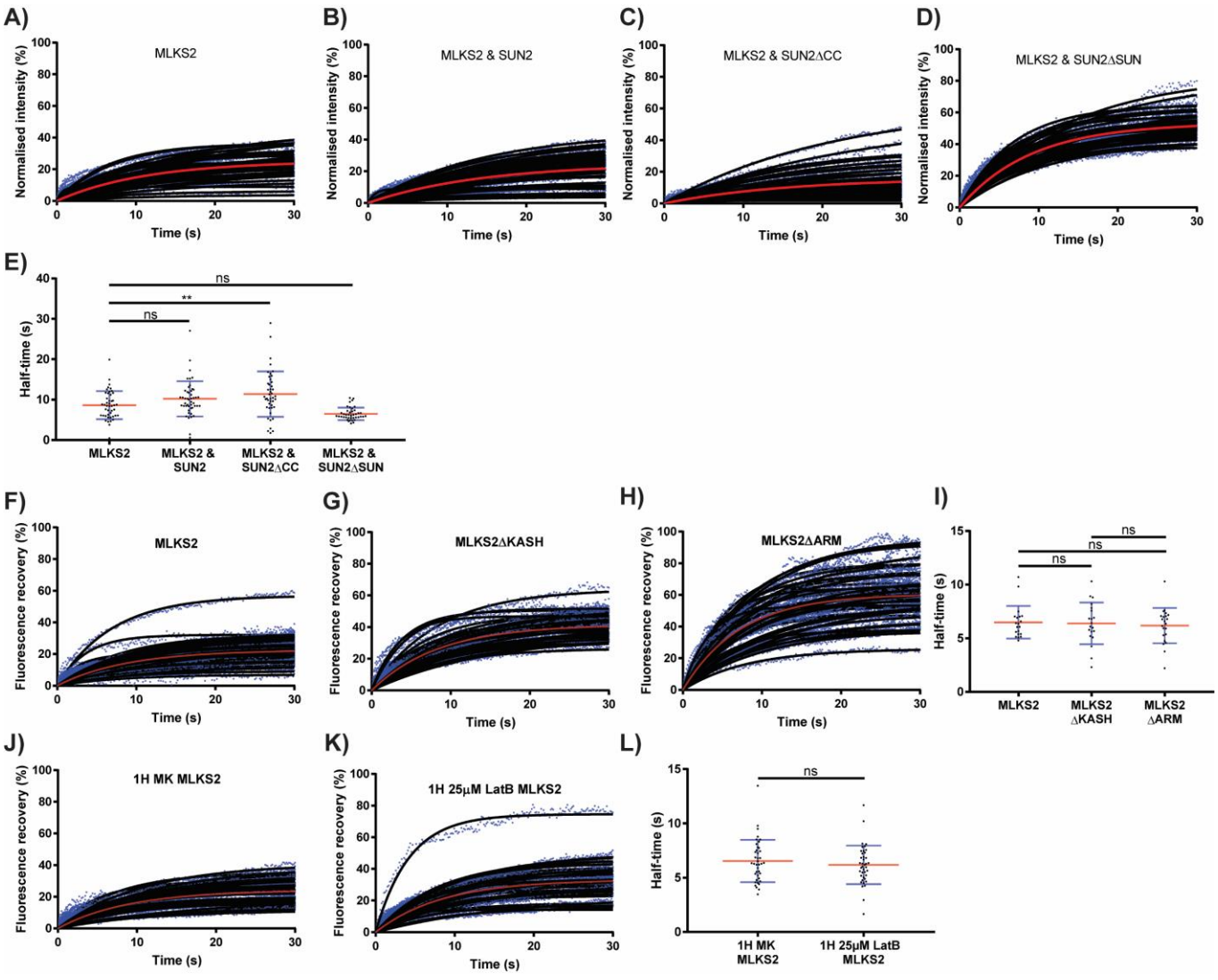
A)
MLKS2
Normalised intensity (%)
Time (s)
B)
MLKS2 & SUN2
C)
MLKS2 & SUN2ΔCC
D)
MLKS2 & SUN2ΔSUN
E)
Half-time (s)
ns
**
ns
MLKS2
MLKS2 & SUN2
MLKS2 & SUN2ΔCC
MLKS2 & SUN2ΔSUN
F)
MLKS2
Fluorescence recovery (%)
G)
MLKS2ΔKASH
H)
MLKS2ΔARM
I)
ns
ns
ns
MLKS2
MLKS2 ΔKASH
MLKS2 ΔARM
J)
1H MK MLKS2
K)
1H 25μM LatB MLKS2
L)
ns
1H MK MLKS2
1H 25μM LatB MLKS2

Figure S1

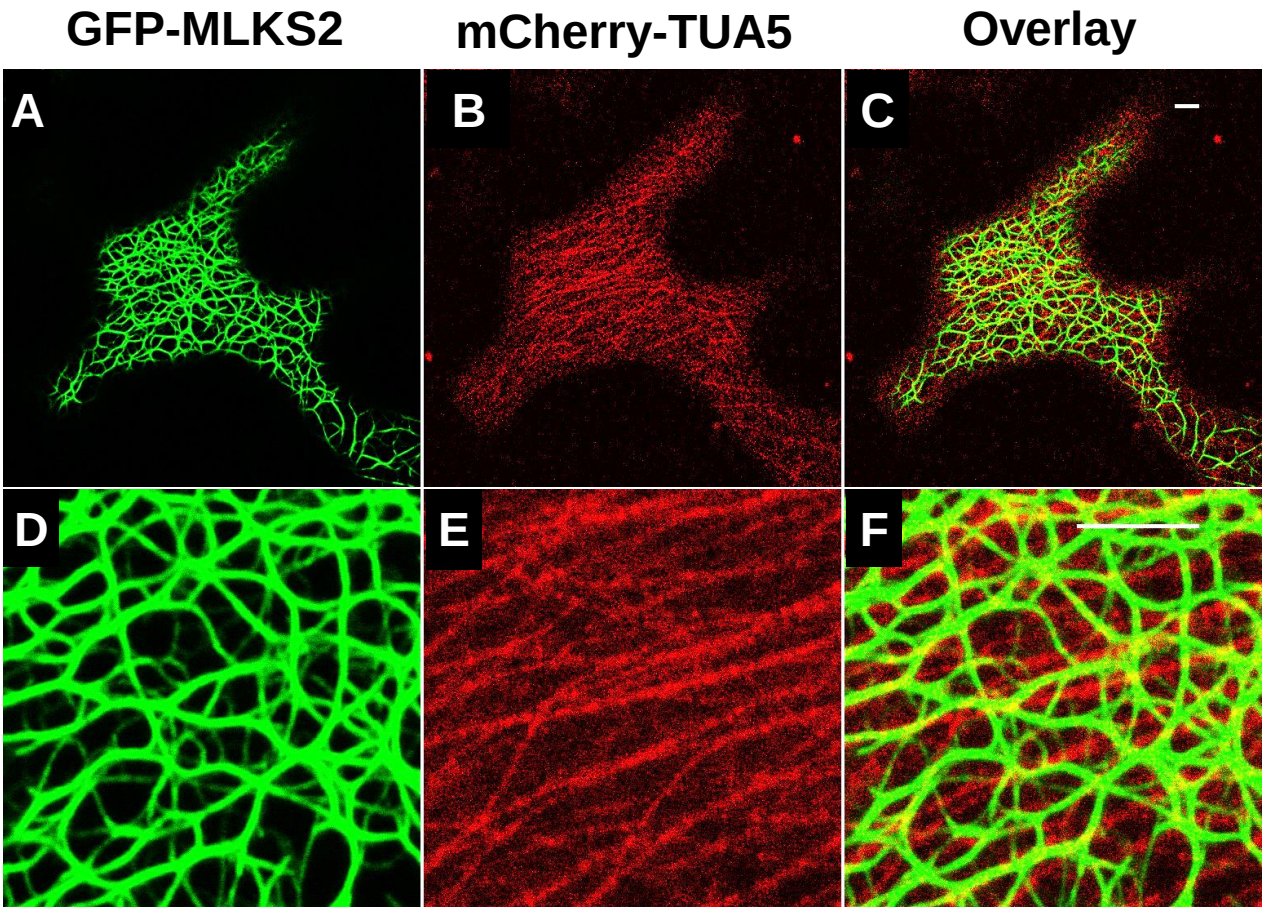

Figure S2

Table S1. Plasmid information (Gumber et al.)

	Plasmid name	Alternate lab name	Construct	Vector backbone	Antibiotic marker	Deletion
Synthetic construct Genscript	pHWBF08		eGFP-FLAG-HA-MLKS2	pUC18	Amp	none
Full length MLKS2 entry clone	MLKS2ec	pPK1F-EC	eGFP-FLAG-HA-MLKS2	pDONR221	Kan	none
Full length MLKS2 expression clone	MLKS2exp	pPK1Fexp	eGFP-FLAG-HA-MLKS2	pH7WG2	Sm/Sp	none
Deletion construct entry clones	MLKS2del4ec		eGFP-FLAG-HA-MLKS2del4	pDONR221	Kan	terminal 4 amino acid residues
	MLKS2delKASHec	pPK1FdelKASHec	eGFP-FLAG-HA-MLKS2delKASH-AA/	pDONR221	Kan	KASH domain
	MLKS2delTMec	pMLKS2delTMec	eGFP-FLAG-HA-MLKS2delTM	pDONR221	Kan	transmembrane domain onwards
	MLKS2delARMec	pMLKS2delARMec	eGFP-FLAG-HA-MLKS2delARM	pDONR221	Kan	ARM domain
Deletion construct expression clones	MLKS2del4exp	pPK1Fdel4exp	eGFP-FLAG-HA-MLKS2del4	pH7WG2	Sm/Sp	terminal 4 amino acid residues
	MLKS2delKASHexp	pPK1FdelKASH-AAAexp	eGFP-FLAG-HA-MLKS2delKASH-AA/	pH7WG2	Sm/Sp	KASH domain
	MLKS2delTMexp	pPK1FdelTMexp	eGFP-FLAG-HA-MLKS2delTM	pH7WG2	Sm/Sp	transmembrane domain
	MLKS2delARMexp	pPK1FdelARMexp	eGFP-FLAG-HA-MLKS2delARM	pH7WG2	Sm/Sp	ARM domain

Table S2. List of primers used for construct cloning (Gumber et al.)

Plasmid genera	Name	Sequence (5'-3')	Purpose
MLKS2-EC	BPHWB8F	GGGGACAAGTTTGTACAAAAAAGCAGGCTTCATGGTCTCCAAGGGCGAGG	att primers to amplify eGFP-MLKS2 for creating entry clone
	BPHWB8R	GGGGACCACTTTGTACAAGAAAGCTGGGTCTCAGGTCGGCACCAGGTACG	"
MLKS2ΔARM	1Fdel4F	AAGGGCCTCGTCATTTCTTCAGAGCAGATGC	To generate MLKS2delARM entry clone
	1Fdel4R	CCCCATGCCAGCCCCGGC	
MLKS2Δ4*	1Fdel1F	TGAGACCCAGCTTTCTTGTAC	To delete terminal nucleotide bases corresponding to LVPT
	1Fdel1R	GTACGCGCTGTCATCGTC	
MLKS2ΔKASH*	1Fdel2F	CGCATGAGACCCAGCTTTCTTG	To delete terminal 42 bases corresponding to TMD and add 9 bases corresponding to 3 alanines
	1Fdel2R	GCAGCGATCAGCATCGTAATGATAG	
MLKS2ΔTM*	1Fdel3F	TGAGACCCAGCTTTCTTGTACAAAG	To delete bases TMD onwards
	1Fdel3R	CTTCGCGCGGTACTTCCG	

Table S3. List of genotyping primers (Gumber et al.)

Primers used for genotyping

Primer name	Alternate lab name	Sequence 5'-3'
gF1	mu1038603F1	GGAGGCGTACGCGAGGTCCA
gR1	mu1038603R1	GAGGCTCCGGCATGGGCTCT
gF2	mu1056535F2	ATTCATCCATCATGAACGGCAGCAC
gR2	mu1056535R2	CTGGGACTGGGAGTCTTGTCCCTTG

Primers used for qRT-PCR

qF1	qS2F1	AAGGGACAAGACTCCCAGTCC
qR1	qS2R1	GAGCTTTGAAGCAATCGGAGA
qF2	qS2F2	CCACTACCGAGGCTGAGAACA
qR2	qS2R2	TGGTCTTCCCTATGCTGCTTG
qF3	qS2F3	AAGATGACTTGGGCGAGGTCT
qR3	qS2R3	GAACCATTGTGGCTTGGTGAC